UNIVERSITY OF CAMBRIDGE
Chemical Engineering and Biotechnology

Modelling the behaviour of a stationary horizontal liquid jet impinging on a vertical wall

A dissertation submitted to the University of Cambridge for the degree of Master of Philosophy in Advanced Chemical Engineering (ACE)

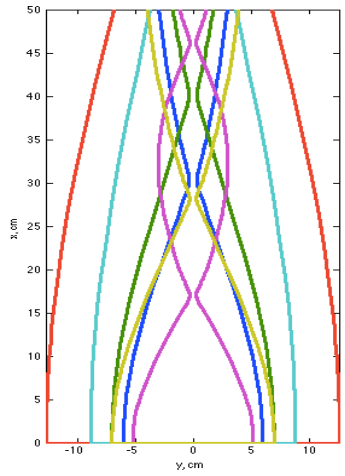

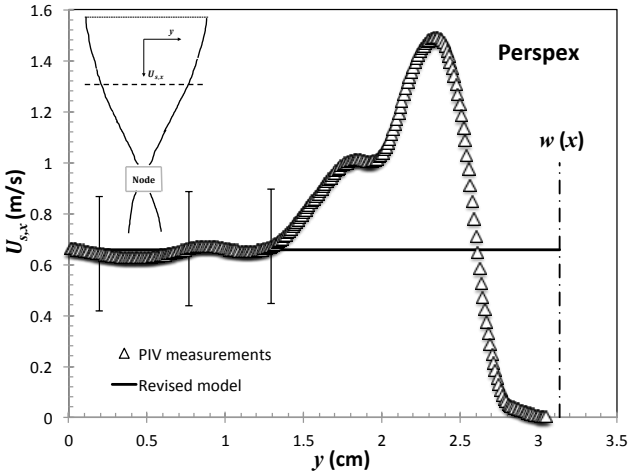

Presented by

Wassim Aouad

St Edmund's College

University of Cambridge

22 August 2014

Preface

This dissertation is submitted in partial fulfilment of the requirements for the degree of Master of Philosophy in Advanced Chemical Engineering in the Department of Chemical Engineering and Biotechnology of the University of Cambridge. It documents the research work simultaneously performed in the Department of Chemical Engineering and Biotechnology and the GK Batchelor Laboratory at the Department of Applied Mathematics and Theoretical Physics (DAMTP).

The work contained in this dissertation, or any part thereof, has not been submitted for any other degree. This report was submitted on the 22nd of August 2014 and contains 10,000 words.

The author would like to express his strong appreciation for the generous support and important feedback from his project supervisors, Dr Ian Wilson and Prof John F. Davidson, as well as Dr Julien Landel and Dr Stuart Dalziel at DAMTP.

The author would also like to take advantage of this opportunity to express his infinite gratitude to his family for the support and faith in his abilities since childhood.

A manuscript is currently being prepared for submission to the *Journal of Fluid Mechanics*, containing the results presented in this dissertation.

Abstract

Predicting the flow patterns generated by liquid jets impinging on vertical surfaces is crucial for designing efficient industrial tank cleaning systems. The flow behaviour generated by a stationary horizontal water jet impinging on a vertical target surface (Perspex, glass or polypropylene) was investigated. The work was studied experimentally and numerically (modelling). The jets were generated by nozzles similar to those used in industrial cleaning, with diameters ranging from 2 to 4 mm. The jet velocity varied from 1.89 to 12.2 m s^{-1} for flow rates between 0.48 and 4 L min^{-1}. Particle image velocimetry (PIV) was used to give detailed information about surface velocity distributions.

Existing models for the impingement region gave reasonable predictions of the flow pattern. However, marked disagreement was found between the velocity field derived from these models and the velocities measured by PIV. The Nusselt thin film assumption, generally used when the flow is laminar and uniform, was found to be inaccurate as the flow is wavy and unsteady.

The modelling of the draining film zone was based on the work of Mertens *et al*. (2005). This model was found to predict a negative film thickness due to the use of a quartic function for the height distribution. PIV measurements revealed that Mertens *et al*.'s assumption of a uniform velocity across the entire cross-section at a given vertical location was inaccurate. The draining film zone possesses a flat central region where the velocity is uniform, whereas the outer region, called the rope, is characterized by a relatively large thickness and a non-uniform velocity profile. Waves were also detected on the surface of the falling film, which led to interrogate the validity of the Nusselt falling film assumption used by Mertens *et al*. (2005) to derive the model.

An alternative boundary condition based on capillary force alone was proposed for Mertens et *al*.'s model and this gave a good prediction of the narrowing pattern as well as the velocity field. The results highlighted the importance of the receding contact angle.

Table of Contents

1.0 Introduction

1.1 Importance of cleaning in industry

The cleaning of soiled equipment is a critical stage in many industrial processes, such as those found in the food and pharmaceutical sectors, particularly when fouling occurs and when dealing with batch-based operations during which several products are manufactured on one plant using the same tanks or vessels (Wilson *et al*., 2012). Industrial cleaning is a crucial operation since it affects the final quality of the product, degree of cross-contamination and batch integrity (Detry *et al*., 2009).

Soil (or residual product film) removal can be achieved by filling (or immersing) the entire tank with a solution containing a detergent, by allowing it to soak for a certain length of time, and by draining the detergent subsequently. However, this technique is time and material consuming and depends strongly on chemical and thermal (temperature) considerations (Jensen *et al*., 2011-2012). A common, and more efficient, method for cleaning equipment in industry is the application of a cleaning liquid by jets from a spray ball or nozzle (Morison and Thorpe, 2002). Spray balls and nozzles can be either static (Figure 1) or rotating.

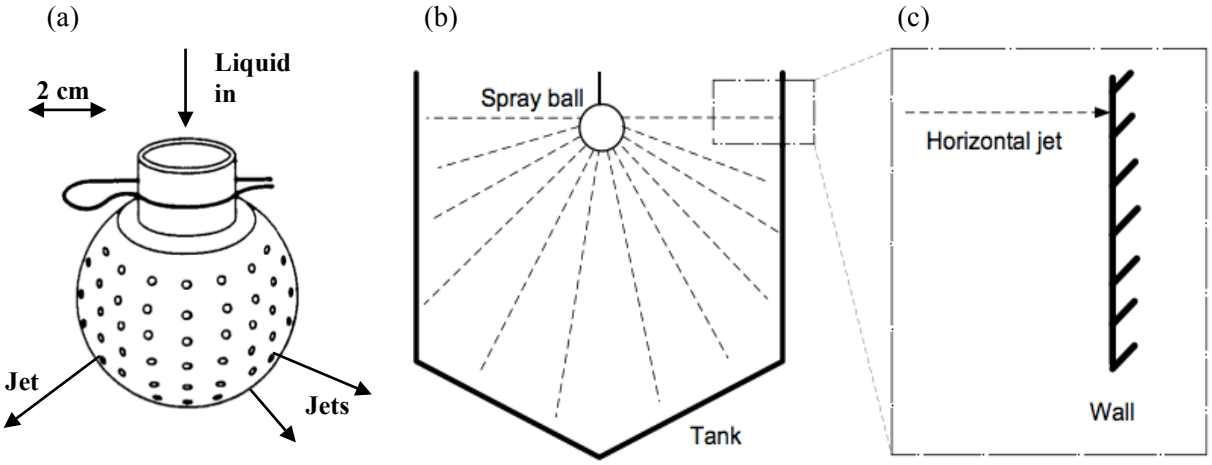

Figure 1. Static spray ball cleaning system. (a) Typical spray ball used for cleaning purposes (Morison and Thorpe, 2002). (b) Schematic cross-section of a tank cleaning system. (c) Horizontal jet impinging on tank wall.

This Cleaning-In-Place (CIP) technique uses high-pressure jets (Wilson, 2005) that impinge on the soiled surface, creating impact forces at the contact point as well as shear stresses over a larger region of the wall as the liquid spreads and drains, contributing to the removal of soil. In this context, it is important to understand the theory of the complex flow generated on the surface in order to design efficient cleaning systems. Predicting the size and shape of the wetted area created by the

impingement of liquid jets is of importance for designing cleaning systems and evaluating their cleaning efficiency.

1.2 Flow behaviours generated by impinging jets

The flow patterns generated by impinging liquid jets have been reported in several studies. Once a horizontal jet impinges on a vertical surface (Figure 1(c)), the fluid initially flows radially away from the point of impingement and subsequently falls downwards, as illustrated by Figure 2. Four zones can be distinguished.

Zone I, the Radial Flow Zone (*RFZ*), is centred at the point of impingement. In this zone, the liquid spreads quickly away from the impingement point before forming a *film jump*, which is similar to a hydraulic jump, indicating the transition to a slower flow zone, named the *corona* or *rope* (zone II), in which gravity effects become dominant (Wang, 2014). At the mid-plane (X-X), the radius of the *RFZ* is labelled R and the outer radius of the *corona* is indicated by R_c. Above the mid-plane, the maximum height of the *film jump* is given by Z_r and the maximum height of the *corona* is Z_t (Figure 2). Below the mid-plane, liquid is no longer decelerated by gravity and the film jump is no longer distinct. Liquid flowing radially outwards joins the corona and there is a transition to a falling film. The end of this zone III is located at approximately R below the point of impingement (Wang *et al*., 2013a).

Zone III is also characterized by a radial flow from the impingement region (horizontal and vertical momentums). However, the effect of gravity in this region becomes important and the draining film behaviour starts to take place (Tan, 2012).

Finally, the last region, zone IV, occurs when addition of outward horizontal momentum has stopped and the liquid film starts to drain downwards. The transition between zones III and IV is characterized by the liquid attaining a maximum width, shown by W in Figure 2, since no more forcing radial flow is being added to the flow.

In terms of cleaning efficiency, the high velocities in zones I and III imply that the shear forces imposed by the liquid on the surface are high, which is useful for cleaning purposes, whereas the relatively low velocity in zones II and IV suggests that the rate of any shear-driven mechanism will be slower there. Knowledge of these regions is important for wetting, as this can lead to softening of the soil layer and cleaning by different methods.

(a) (b)

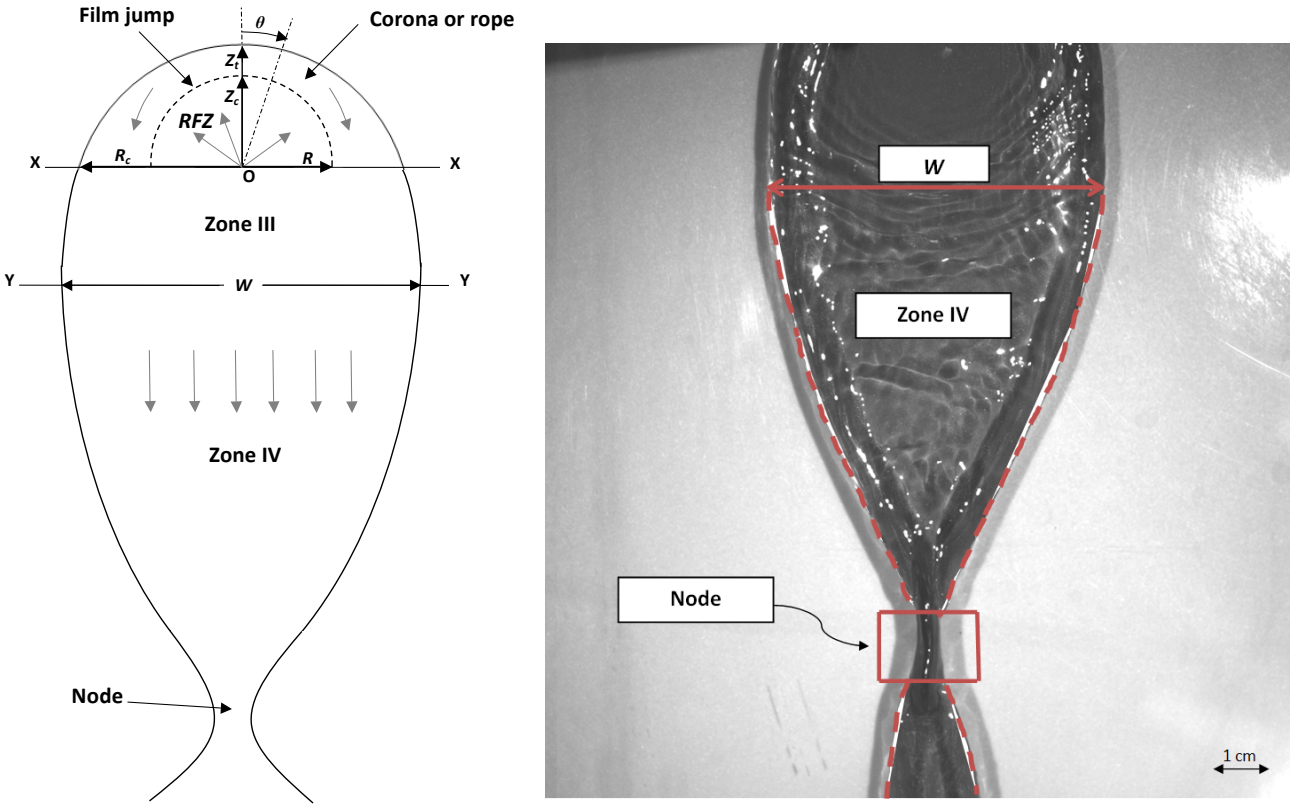

Figure 2. Flow patterns generated by liquid impinging on a vertical wall. (a) Schematic. (b) Photograph illustrating the narrowing pattern in zone IV. Water flow rate at 0.5 L min^{-1}, Perspex sheet. Dashed lines indicate the flow shape.

In general, the flow behaviour of draining films can be classified into two types: *gravity flow* and *rivulet flow* (Wilson *et al*., 2012). The latter refers to the case in which the falling film takes on the shape of a thin strand where surface tension effects are comparable to gravity contributions. In gravity flow, the draining liquid forms a uniform, wide falling film when gravity contributions dominate the surface effects, such as the surface tension and contact angle.

For surfaces that are not perfectly wetting, these surface effects determine the behaviour of the falling film, as reported by Mertens *et al*. (2004). Once the liquid reaches its maximum width, *W* (boundary between zone III and IV), the film starts to narrow and a series of narrowing and widening patterns, or braids, are observed. Figure 2 illustrates the formation of one braid. This can be explained by the fact that surface tension limits the extent of spreading and pushes the outer edges of the flow inwards, which causes the film to narrow. As the film contracts to form a *node* (Figure 2),

the outer boundaries accelerate beyond equilibrium and bounce on impact, forcing the liquid to expand outwards. Subsequently, the liquid starts narrowing again due to surface tension, and the process is repeated (Mertens *et al*., 2004).

The width of the braids becomes smaller because of energy dissipation due to friction. Therefore, the aim of the present work is to model the flow pattern in the first braid (i.e. until the first node is reached) since it forms the most critical region for cleaning purposes.

Finally, gravity flow behaviour can be accompanied by the formation of dry patches that split the falling film into several strands. These dry patches are to be avoided in cleaning as they allow the accumulation of fouling layers since the dirt will not be removed from these regions (Paramalingam *et al*., 2000).

The transition between the rivulet and gravity flow behaviour is dependent on the flow rate (Mertens *et al*., 2004). For high flow rates, gravity flow is observed. In terms of cleaning efficiency, rivulet flow behaviour results in a small wetted area with an unpredictable path whereas gravity flow gives a large wetted area (Tan, 2012). Thus, gravity flow is desirable for cleaning purposes.

1.3 Objectives of the project

The present work aims to model the flow pattern of a stationary horizontal jet impinging on a vertical wall, with an emphasis on zone IV since the impingement zone has been previously studied by workers in the Department of Chemical Engineering and Biotechnology. The wetting behaviour of liquid jets from spray balls is studied by considering a single horizontal coherent jet of water impinging on a vertical surface. The main objective of this study is to predict the narrowing width of the liquid film in the draining film zone. This is achieved by the modification of existing mathematical models that were found to contain invalid assumptions. Additionally, the reproducibility of the results using existing models for the impingement zone is also investigated in order to present a full description of the flow. The validity of these models is tested using particle image velocimetry (PIV) in order to compare the measured velocity distributions with those predicted by the existing models.

2.0 Background

As mentioned above, this work concentrates on the draining film region. Nonetheless, presenting and evaluating the validity of existing models describing other regions is needed in order to provide a full description of the flow behaviour.

2.1 Modelling of zone I: R and Z_r

Several models have been proposed for predicting the value of the radius of the radial flow zone at the mid-plane, R. Wilson *et al*. (2012) developed an expression based on momentum and force balances, neglecting the effect of gravity and assuming a Nusselt thin film (i.e. parabolic velocity profile) to simplify the relationship between the shear stress and the velocity. The force balance is similar to the one employed in section 4.4 in the present study. In this model, the momentum in the radial direction is balanced by the surface tension force opposing wetting, thus giving the location of the film jump at the mid-plane, R, as:

$$R = 0.276 \left[\frac{\dot{m}^3}{\mu\rho\gamma(1-cos\beta)}\right]^{\frac{1}{4}}, \tag{1}$$

where ρ is the liquid density, $\dot{m}$ the mass flow rate, μ the dynamic viscosity, γ the liquid-vapour surface tension and β the contact angle between the liquid, vapour and the surface. Wilson *et al*. (2012) also assumed that the initial film mean velocity termed U_o, which is equal to the mean velocity of the jet (Watson, 1964), is much higher than the film mean velocity at R, U_R, and that the jet radius, r_o, which is equal to the nozzle radius, is much smaller than R.

Wang *et al*. (2013a) extended the analysis of Wilson *et al*. (2012) for predicting R and used the same momentum and force balances but included the effects of nozzle size by considering U_o and r_o. Their modified model for predicting R was:

$$\frac{3\dot{m}^3}{5\pi\rho\gamma R(1-cos\beta)} = \pi r_o^2\dot{m} + \frac{10\pi^2\mu}{3}[R^3 - r_o^3]\,. \tag{2}$$

Another key parameter in the radial flow zone is the maximum height of the film jump Z_r. Z_r is less than R because gravity retards the upward flow. Hence, Wang *et al*. (2013b) developed a model that takes gravity into account. For a streamline, using a momentum balance similar to that employed by Wilson *et al*. (2012) gives a differential equation linking the local velocity U with the radial position r:

$$\frac{d}{dr}U = -10\pi^2\frac{\nu U^2 r^2}{q^2} - \frac{5g\,cos\theta}{6\,U}, \qquad \text{(gravity model)} \tag{3}$$

where q is the total volumetric flow rate, ν the kinematic viscosity, g the gravitational acceleration and θ the angle of inclination of the streamline to the vertical, as indicated in Figure 2(a). The local velocity U as a function of r is obtained by integrating (3) using the boundary condition $U = U_o$ at $r = r_o$.

As with the above models, the flow stops spreading out, creating the film jump, when the radial momentum is balanced by the inward force due to surface tension. Using a force balance gives the following expression for the mean velocity at the film jump:

$$U(r) = \frac{5\pi\gamma(1 - cos\beta)}{3\rho q} r \,. \tag{4}$$

Hence, Z_r is found by integrating (3) for $\theta = 0^o$ ($cos\theta = 1$) to give $U(r)$ and finding the radial position which satisfies (4) by solving numerically to find Z_r.

2.2 Modelling of zone II: R_c and Z_t

The correlation for the outer radius of the corona, R_c, was previously reported and empirical relationships between R and R_c were identified based on experimental observations. For instance, Wilson *et al*. (2012) found that $R_c \approx 2R$ for water at lower flow rates (up to 2 g s^{-1}) whereas R_c approached $4R/3$ in the experiments conducted by Morison and Thorpe (2002), which employed higher flow rates ($9 \leq \dot{m} \leq 88$ g s^{-1}).

Regarding Z_t, Wang *et al*. (2013b) derived a model for the width of the rope region (zone II). In this model, the liquid flow is deemed to be proportional to the angular coordinate θ because the rope is fed with radially flowing water from the jet. The model is derived from a momentum balance on an element of rope, assuming negligible wall shear. After some simplifications and integration from $\theta = 0^o$, the width of the rope as a function of the angular position θ is obtained by assuming that the rope possesses a semi-circular cross-section:

$$D\,(\theta) = \frac{2}{\pi}\sqrt{\frac{q}{\sqrt{2gR}}}\sqrt{\frac{\theta}{\sqrt{f_{rope}(\theta)}}}\,, \tag{5}$$

where $f_{rope}(\theta)$ is given by:

$$f_{rope}(\theta) = \frac{2\,sin\theta}{\theta} + \frac{2(cos\theta - 1)}{\theta^2} cos\theta \,. \tag{6}$$

In order to get the width of the rope necessary for the calculation of Z_t, the value of θ in equations (5) and (6) is set to 1^o (since 0^o is mathematically impossible due to the presence of θ in the denominator). Z_t is then given by:

$$Z_t = Z_r + D(\theta = 1^o) \,. \tag{7}$$

2.3 Modelling of zone III

There are no existing models for predicting the different parameters in zone III, such as the shape, the velocity profile and the width. This region was experimentally investigated by Wang *et al*. (2013a).

They reported that zone III, which is characterized by the presence of a radial flow from the jet, is defined over a downward distance equal to *R* below the impingement plane. Hence, beyond this level, momentum from the impingement point is no longer added to the film, marking the transition to zone IV where the film is expected to narrow due to surface tension for liquids which do not wet the surface perfectly (a maximum width is reached at the interface between zones III and IV).

2.4 Modelling of zone IV

This region was studied experimentally and a model was presented by Mertens *et al*. (2005). A critique of their model is presented in section 4.

2.5 Advancing and receding contact angles

Following the analysis of Wilson *et al*. (2012), determining the relevant contact angle value (i.e. advancing or receding (retreating) contact angle) is of importance in such flows where different zones have different behaviours. They reported that in a stable flow, the advancing contact angle is likely to be the relevant value for the impingement zone (zone I and II) while Wang et *al*. (2013a) mentioned that both values are expected to be important in the draining film region (zones III and IV), depending on whether the width is increasing (zone III) or decreasing (zone IV). These statements are based on the argument that in zones II and III, the liquid is actively wetting the surface, therefore advancing on the surface, whereas in zone IV, the liquid is de-wetting or retreating, therefore receding from the surface (and the width is narrowing).

Advancing and receding contact angles can be either static or dynamic. Dynamic contact angles are manifested when the liquid is moving. These contact angles depend on both the speed and direction of the contact line displacement (Blake, 2006). Therefore, the dynamic contact angles are probably the ones that should be used in the impinging jet models. Evaluating these contact angles is complex, however, since they are velocity-dependent. According to Le Grand *et al*. (2005) who investigated the dynamic case, the advancing contact angle increases with liquid speed, while the receding angle decreases.

3.0 Experimental procedures

Impinging jet apparatus and experiments

A coherent horizontal liquid jet impinging on a vertical surface was generated in the apparatus shown in Figure 3. Water, dyed blue and containing tracer particles in the case of PIV experiments, was

pumped to form a liquid jet coming out of a nozzle. The angle between the jet and the surface was checked periodically by means of an electronic inclinometer. The pressure upstream of the nozzle was measured using a manometer and employed to monitor the flow rate, which was determined via separate catch-and-weigh calibration tests and compared with rotameter measurements. Three stainless steel nozzles, with inner convergent angle of 45° and orifice diameters d_N of 2 mm, 3 mm and 4 mm, were used. Three different transparent surfaces were employed: Perspex, glass and polypropylene-covered plates. The distance between the nozzle and the surface, *l,* was maintained at approximately 5 cm, a relatively small distance, in order to ensure that coherent jets were generated with no beak-up into droplets. The flow rate was varied from 0.48 L min^{-1} to 4 L min^{-1} and the jet Reynolds number, $Re_{jet} = \rho U_o r_o/\mu$, ranged from 4.23×10^3 to 28.2×10^3. These values are lower than the ones employed in industrial tank cleaning systems ($Re_{jet} \approx 10^5$) (Jensen, 2014). Liquid draining from the plate was recycled back to a tank and a pump recirculated the liquid into the apparatus.

The target was cleaned with soap and distilled water between tests. Isopropanol was subsequently used to remove any further contamination. During each experiment, steady state conditions were attained before photographing the flow pattern using a Canon DIGITAL IXUS 75 camera located in front of the target, similar to the situation shown in Figure 3 (a).

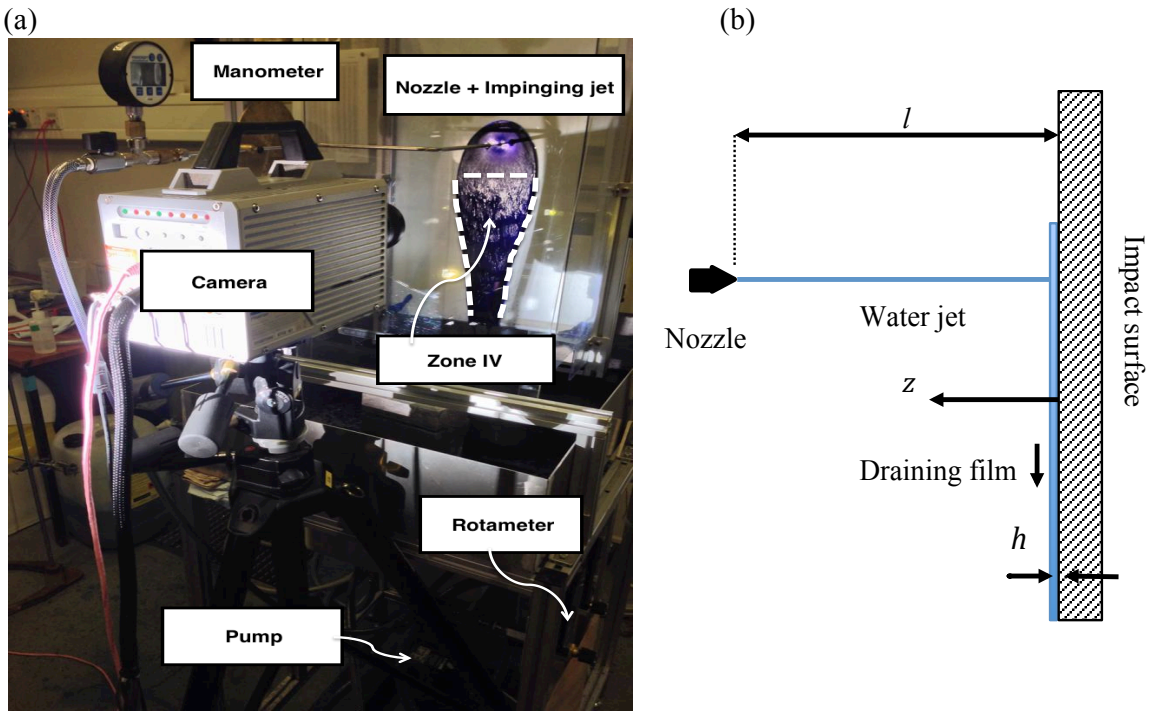

Figure 3. Impinging jet apparatus. (a) Photograph of the apparatus. (b) Schematic, side view.

Contact angle measurements were made at the Institute of Biotechnology in Cambridge using the standard procedures for evaluating advancing and receding contact angles, except that the droplets were pipetted manually using a micropipette. The advancing contact angle was determined by adding volume to the drop continuously, up to the maximum volume permitted without moving the contact line between the liquid and surface, whereas the receding contact angle was measured by removing the liquid from the large drop without moving the contact line.

Contact angle measurements were made with a DataPhysics Optical Contact Angle (OCA) measurement device. The system was connected to a desktop PC (Windows XP, 2.5 GHz, 1.99 GB RAM). Image processing was conducted using OCA 20 software that automatically measures the angles. The user specifies the location of the surface, and the software fits a curve around the droplet before extracting the contact angle by inspecting the tangent at the solid-liquid-vapour interface.

PIV was employed to investigate the velocity field in the different zones of the flow. This non-intrusive technique allows measurements of the two-dimensional instantaneous surface velocity of the film (in the x and y directions) by a high-speed camera that detects the movement of tracer particles (Landel and Dalziel, 2014). A dye was added to the liquid to obtain an opaque fluid (Figure 4(a)), masking tracer particles beneath the surface. The images taken by the camera were analysed using *DigiFlow* (Dalziel *et al*., 2007). The PIV experiments were recorded using a high-speed grey-scale camera (Photron-Fastcam SA1.1) fitted with a 60 mm focal length AF Micro-Nikkor lens. The lens aperture was adjusted to avoid over-illumination. Table 1 summarizes the control parameters used in the experiments. These experiments were assisted by Drs Stuart Dalziel and Julien Landel from the Department of Applied Mathematics and Theoretical Physics (DAMTP).

Methylene blue (Fisher Scientific) was chosen as the dye (concentration: 6.5 g L^{-1}). Pearlescence (Iriodin 120 pigment, Merck), made of titanium-dioxide coated mica particles (density: 3 g cm^{-3}, size: 5 to 25 microns) that possess a flat plate shape and exhibit silver-pearl colour when mixed with water, was selected as the tracer particle (volume fraction: 0.17%). The viscosity of the methylene blue solution was measured using an ARES controlled strain rheometer (Rheometric Scientific) using a smooth couette cell and found to be similar to that of water.

Table 1. Control parameters used in the PIV experiments.

Zone (-)	Resolution (pixel x pixel)	View (cm x cm)	Recording rate (frame s^{-1})	Shutter opening (s)	Lens aperture (-)
I	512 x 512	6 x 6	20000	1/30000	f/4.0D
IV	1024 x 1024	12 x 12	5400	1/30000	f/4.0D

4.0 Model development

4.1 Mertens *et al.*'s model for the braiding pattern of a stream

4.1.1 Height function and capillary force

This section is mainly based on the paper by Mertens *et al*. (2005) who were interested in liquid films flowing down inclined rock faces. In this study, the coordinate system is set as follows (Figure 4): the x-axis points downwards along the draining surface and the y-axis is horizontal to this, in the plane of the surface, while the z-axis is oriented normal to the surface in the direction of the film thickness (height h). The flow is symmetric with respect to the *(x-z)* plane, so the model is written in terms of the half-width of the film, w, and half the flow rate, Q.

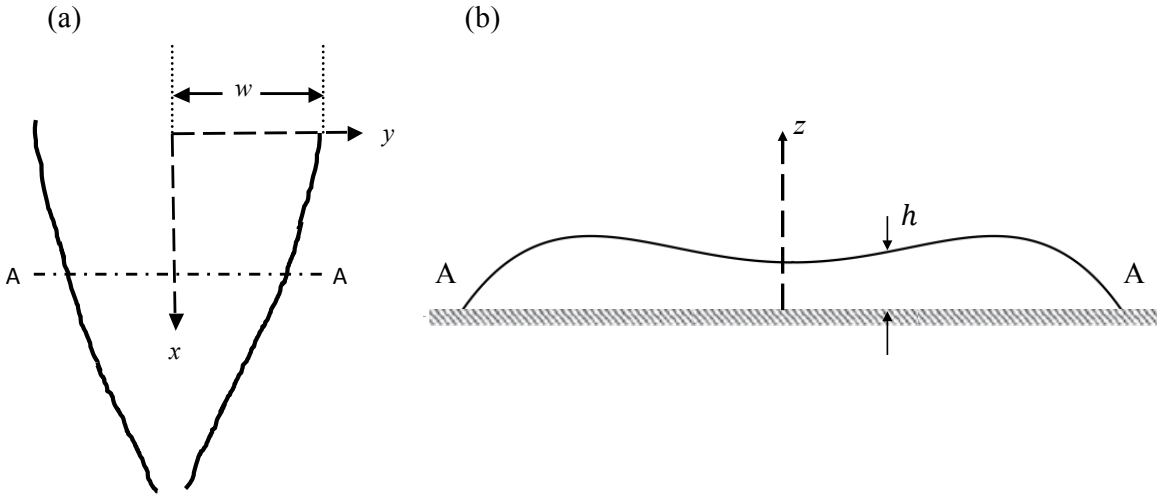

Figure 4. Schematic diagram showing the Cartesian coordinate system used for modelling the braiding pattern. Solid lines represent the flow shape. (a) x-axis and y-axis. (b) View of the cross section at A-A as predicted by equation (8): z-axis.

Mertens *et al*. hypothesised that the film height at distance x down the plane can be written as a quartic function of y:

$$h(x,y) = (w^2 - y^2)(a - by^2)\,, \tag{8}$$

where a and b are constants to be determined.

Assuming that the x component (U_x) of the velocity dominates the flow and is uniform in the y direction (independent of y), the half flow rate Q is given by the flux condition:

$$Q = U_x \int_0^w h(x,y)dy = constant\,. \tag{9}$$

The coefficient a is found by differentiating (8) and relating it to the shape at the contact line:

$$\frac{dh(\pm w)}{dy} = \mp tan\beta\,. \tag{10}$$

Mertens *et al*. did not specify which contact angle is to be used in the model. Physical arguments suggest that the receding contact angle applies here since the liquid is receding from the surface and the width is decreasing, as mentioned in section 2.5. This gives:

$$a = \frac{tan\beta}{2w} + bw^2. \tag{11}$$

The coefficient b is obtained by substituting (8) and (11) into (9), followed by integrating the latter and isolating b:

$$b = \frac{15}{8w^5}\left(\frac{Q}{U_x} - \frac{w^2 tan\beta}{3}\right). \tag{12}$$

The capillary force, F, acting inwards on the half-braid and causing it to narrow is then given by:

$$F = \gamma \int_0^w h(y)h'''(y)dy\,. \tag{13}$$

Evaluating this integral gives the capillary force:

$$F = \gamma(3bw^3 tan\beta + 4b^2w^6) = \gamma F^*, \tag{14}$$

where $F^*$is the dimensionless form of F.

4.1.2 Equations of motion used for modelling the braiding pattern

The boundary layer approximation is used to simplify the Navier–Stokes equations (keeping the second derivative with respect to z):

$$\boldsymbol{U}.\nabla\boldsymbol{U} = \frac{1}{\rho}\nabla p + g\hat{\boldsymbol{e}}sin\alpha + \nu\frac{\partial^2\boldsymbol{U}}{\partial z^2}, \tag{15}$$

where $\boldsymbol{U}$ is the three-dimensional velocity vector (the z component is neglected), $\hat{e}$ is the unit vector in the direction of flow, α is the angle of inclination, and p is the pressure.

Using the integral method and by double-integrating from 0 to w and from 0 to h for a half-braid, the flux condition (9) reduces the equations of motion into two partial differential equations (PDEs) in terms of the x and y components of the velocity; U_x and U_y, respectively:

$$\rho A U_x\left(\frac{\partial}{\partial x}U_y\right) = F - \mu A\frac{1}{h}\frac{\partial U_y}{\partial z}\bigg|_{z=0}, \tag{16}$$

$$U_x\frac{\partial U_x}{\partial x} = gsin\alpha - \nu\frac{1}{h}\frac{\partial U_x}{\partial z}\bigg|_{z=0}, \tag{17}$$

where A is the cross sectional area of a half-braid.

The lubrication approximation is then used to simplify these two equations by assuming a Nusselt falling film (parabolic velocity profile), in addition to considering U_x as a function of x only and replacing h with $h_{avg} = A/w = Q/(U_x w)$. The relationship between U_x and U_y is determined using continuity or mass conservation. Two ordinary differential equations (ODEs) are thus obtained with respect to U_x and w (equations (20) and (21) below). The following scaling variables are used to make the ODEs dimensionless:

$$x = Lx_*, \quad w = Lw_*, \quad U_x = Vu_*\,, \tag{18}$$

where the characteristic length, L, and velocity, V, are given by:

$$L = \frac{\rho^2 Q^2 g sin\alpha}{\gamma^2}, V = \frac{\rho Q g sin\alpha}{\gamma}. \tag{19}$$

The values of the characteristic length and velocity for all the flow rates used in the present study (0.48 to 4 L min^{-1}) are $3 \leq L \leq 209$ and $0.54 \leq V \leq 4.53$.

Finally, a series of simplifications yield two differential equations:

$$\frac{d}{dx_*}\left(u_* \frac{dw_*}{dx_*}\right) = F_* - \Pi_I u_*^2 w_*^2 \frac{dw_*}{dx_*}, \tag{20}$$

$$u_* \frac{du_*}{dx_*} = 1 - \Pi_{II} u_*^3 w_*^2\,, \tag{21}$$

where the dimensionless constants are:

$$\Pi_I = \frac{3\nu L}{Q} = \frac{3\nu\rho^2 Q g sin\alpha}{\gamma^2}, \tag{22}$$

$$\Pi_{II} = \frac{3\nu L^3 V}{Q^2} = \frac{3\nu\rho^7 Q^5 (g sin\alpha)^4}{\gamma^7}. \tag{23}$$

The dimensionless form of Mertens *et al.*'s capillary force is:

$$\mathrm{F}_* = \frac{1}{16}\left[15\frac{\Pi_I}{\Pi_{II}}\frac{1}{u_* w_*^2} - 5tan\beta\right]\left[15\frac{\Pi_I}{\Pi_{II}}\frac{1}{u_* w_*^2} - tan\beta\right]. \tag{24}$$

4.1.3 Critique of Mertens *et al.*'s model

Mertens et *al.*'s model was first investigated by Yu (2013) regarding its effectiveness to model the flow pattern of a horizontal jet impinging on a vertical wall (i.e. the angle of inclination α was set to 90^o). Equations (20) and (21) were solved simultaneously in Matlab™.

Equation (20) is a second order ODE whereas (21) is first order. Thus, three boundary conditions were required to solve the ODEs: (*i*) the maximum width W (= 2w, observed and measured in the experiments), (*ii*) the gradient of the width evaluated at the maximum width level (dw_*/dx_* set equal to zero) and (*iii*) the initial film velocity at the maximum width plane, x = 0 (assumed to be equal to

20% of the jet velocity, an order of magnitude estimate based on the work done by Landel and Dalziel (2013)). Boundary condition (*iii*) is investigated in section 5.

Inspection of equation (24) reveals that this expression for the capillary force is inaccurate if the contact angle between the liquid and the plate is 90°, since the *tan* function is not defined for this angle. For instance, water on a polypropylene sheet possesses an advancing contact angle of 90°. Furthermore, Mertens *et al.*'s model predicts a negative film thickness in some regions of the flow (Figure 5). This physically infeasible feature arises from the form of the quartic function assumed for the height distribution. Finally, as mentioned above, the model assumes that the x component (U_x) of the velocity is uniform across the width of the falling film (independent of y). This assumption is compared with experimental data in section 5.

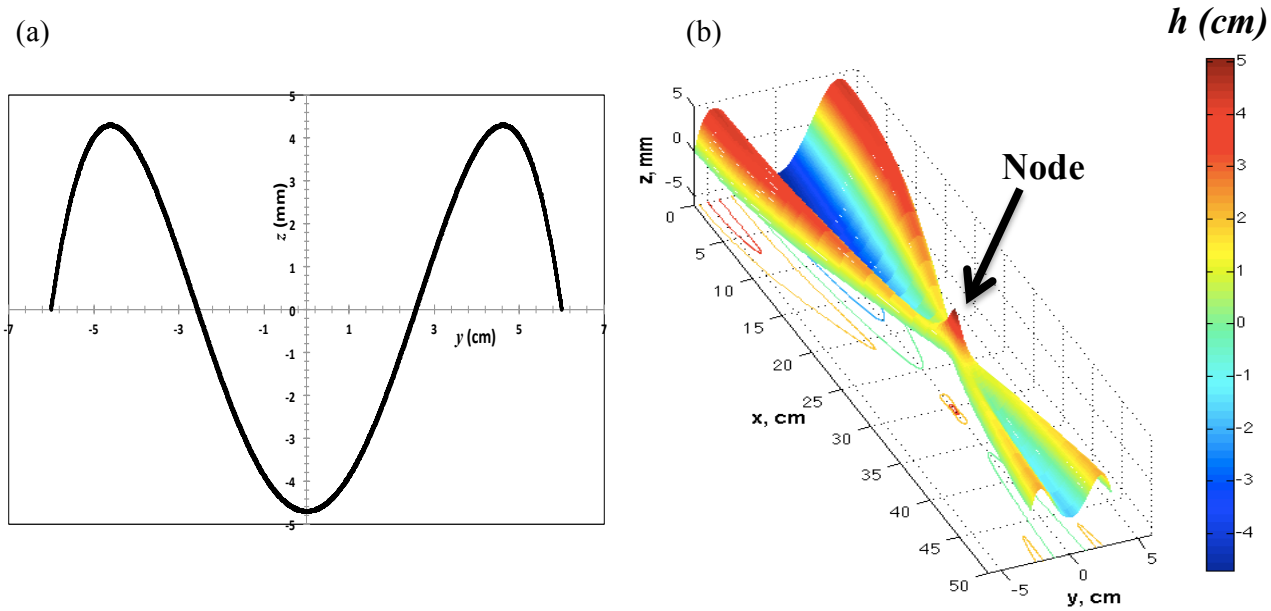

Figure 5. (a) Cross sectional view of the film shape at x = 0 (maximum width) for water flowing at q = 1.5 L min^{-1} on Perspex at 20°C. w = 6 cm is experimental datum. (b) 3-D plot of the film thickness at different positions for the same experiment in (a).

The non-physical height distribution can also be depicted using a 3-D plot of the height over the entire draining film region (Figure 5(b)).

Moreover, the film shape is over-exaggerated compared to the actual profile, which is much flatter in the central region as illustrated by Figure 6, and the magnitude of the height is also over-estimated since the thickness of the draining film is observed to be of the order of 0.5 mm. In reality, the falling film possesses a particular shape: the outer boundaries, called the ropes, exhibit a quasi-circular shape and a relatively large thickness compared to the inner region, which is much flatter and less

thick (Figure 6). Hence, their quartic function for the height distribution does not represent the actual morphology observed experimentally.

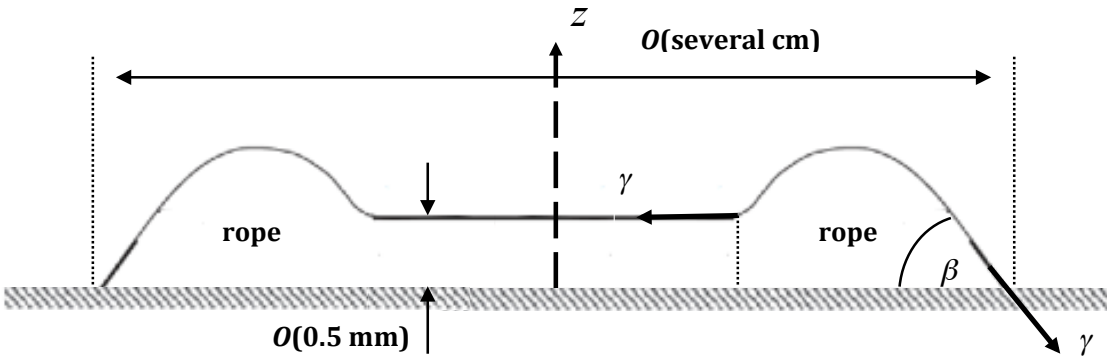

Figure 6. Schematic of a cross sectional view of the falling film. Surface tension forces are illustrated in rope on right.

In terms of the ODEs, the only term affected by the height function is the capillary force expression (equation (13)). Nonetheless, this quartic function has its advantages: it is an even function with respect to z and captures the presence of ropes in the falling film. It also predicts braid formation automatically.

4.2 Alternative capillary force expression

The quartic height distribution (equation 8) in Mertens *et al.*'s original model is problematic: it was replaced here by a simpler one based on observations such as Figure 6. Considering that there is no external source of horizontal momentum in the falling film in zone IV between (Y-Y) and the node (Figure 2) to cause the film to spread out, the film is expected to narrow in response to the surface tension forces acting as shown in Figure 6.

At the outer boundary (i.e. in the ropes), the capillary force acting on the film is that due to surface tension. Hence, equation (14) is replaced by the following net force acting on the half-braid, given by a force balance on one rope:

$$F = -\gamma(1 - cos\beta) = \gamma F^{*}. \tag{25}$$

The negative sign is due to the fact that the capillary force must push the liquid inwards. It is therefore deemed to be negative with respect to the sign convention used in Mertens *et al.*'s model.

This alternative capillary force is used with equations (20) and (21) to give the half-width w as a function of x. This boundary condition predicts the first braid only (until the first node is reached). As mentioned in section 1, the distance to the first node is critical for cleaning purposes.

The only parameter affected by the quartic height function distribution in Mertens *et al.*'s model is the capillary force (see equation (13)). Therefore, replacing Mertens *et al.*'s capillary force by this alternative expression, which does not depend on the height, suggests that the model becomes independent of the film height. Thus, the negative film thickness issue would not be present anymore using the proposed boundary condition.

5.0 Results and discussion

5.1 Fluid physical properties

The models mentioned above require physical properties of water and water-methylene blue-pearlescence (WMP) solution to be determined. Table 2 summarizes the values used in calculations.

Table 2. Liquid physical parameters used in calculations.

Solution	Parameter	Value	Comment/source
water, 25 ^{o}C	Contact angle, β	-	See Table 3
	Density, ρ	997 kg m^{-3}	Measured
	Kinematic viscosity, ν	0.893 10^{-6} m^{2} s^{-1}	(Davis, 2010)
	Surface tension, γ	71.99 10^{-3} N m^{-1}	(Vargaftik et *al.*, 1983)
WMP, 25 ^{o}C	Contact angle, β	-	Similar to Water
	Density, ρ	969 kg m^{-3}	Measured
	Dynamic viscosity, ν	1 10^{-3} Pa s	Measured
	Surface tension, γ	71.99 10^{-3} N m^{-1}	Similar to Water

The measured advancing and receding contact angles of water on Perspex, glass and polypropylene-covered sheet are presented in Table 3. The receding contact angles of water on glass were hard to measure, as they are quite small.

The results in Table 3 show that the advancing and receding contact angles of water on all substrates used are very different. The contact angle hysteresis, defined by $H = \beta_{advancing} - \beta_{receding}$, is relatively large. According to de Gennes (1985), the presence of hysteresis is due to surface roughness, chemical contamination or solutes present in the liquid, such as surfactants or polymers. The values of advancing and receding contact angles present in Table 3 refer to the static case, where the contact line is maintained pinned and there is no flow tangential to the contact line.

Table 3. Advancing and receding contact angles of water on different substrates.

Measurement	Perspex		Glass		Polypropylene	
	Advancing	Receding	Advancing	Receding	Advancing	Receding
1	66.5 º	20.1 º	30.1 º	19.0 º	90.9 º	~35 º
2	71.8 º	24.1 º	36.1 º	8.70 º	90.2 º	~34 º
3	72.2 º	26.2 º	34.3 º	7.20 º	85.9 º	~30 º
4	71.1 º	18.7 º	35.1 º		90.2 º	~30 º
5	70.3 º	21.9 º	39.3 º		99.3 º	~30 º
6	70.0 º	26.4 º	38.7 º		90.4 º	~35 º
7	72.7 º	19.5 º	37.7 º	N.A	88.3 º	-
8	72.0 º	36.5 º	33.7 º		87.6 º	-
9	68.9 º	30.4 º	35.4 º		90.1 º	-
10	71.8 º	28.6 º	40.7 º		89.2 º	-
Average	70.7º±1.9 º	25.2º±5.6º	36.1º±3.1 º	11.6º±6.4º	90.2º±3.6 º	32.3º±5.0º

Zografi and Johnson (1984) found that the advancing and receding contact angles of water on Perspex (PMMA) were 76° and 52° for a smooth surface and 85 ° and 20° for a rough one. The values reported in Table 3 are similar to these. Regarding glass, Chibowski (2003) reported that the advancing and receding contact angles of water on glass were 15° and 0° (perfect wetting), respectively. As for water on polypropylene, Chibowski (2007) mentioned that the advancing contact angle was 91.5° whereas the receding contact angle was 79.7°. Even though these values differ from the measured ones in Table 3, one must keep in mind that each surface has its own characteristics in terms of roughness, contamination, type of polypropylene etc. Contact angle values are very unpredictable and often unrepeatable.

Birch *et al*. (2008) discussed that in industrial cases where metal surfaces are generally used and experience contamination, the advancing contact angles for water vary from 40° to 80° while the receding contact angles are generally smaller than 20°. The contact angle hysteresis is therefore large. Even though this project does not deal with metallic surfaces, these values are quite close to the contact angles reported in Table 3, which adds more industrial relevance to this study.

5.2 Zone I: predictions and measurements of R and Z_r for water

Figure 7 compares experimental results for R with the predictions of the two models, equations (1) and (2), on Perspex for all three-nozzle sizes. The average value of the advancing contact angle on each surface in Table 3 was used in the calculations. Very good agreement is found for the 2 and 3 mm nozzles and reasonably good agreement for the 4 mm nozzle. The discrepancy between the

model and experiments, especially at low volumetric flow rates and low R with the 4 mm nozzle, can be explained by the jet drooping so that it no longer impinged normally on the substrate since the jet velocity is inversely proportional to the nozzle diameter. Comparison of Figures 7 (a) and (b) shows that the two models give similar results. Thus, including the effect of nozzle (U_o and r_o) in the model (equation (2)) does not have a large impact on the prediction of R. Quantitatively similar agreement was obtained for R on glass and polypropylene. This is due to the use of relatively high flow rates in this project, so that the initial film mean velocity, U_o, becomes much higher than the film mean velocity at R, U_R, and the jet radius, r_o, is small compared to R, as assumed by Wilson *et al*. (2012) (equation (1)). Wang *et al*. (2013a) results showed a more significant nozzle effect when using lower water flow rates.

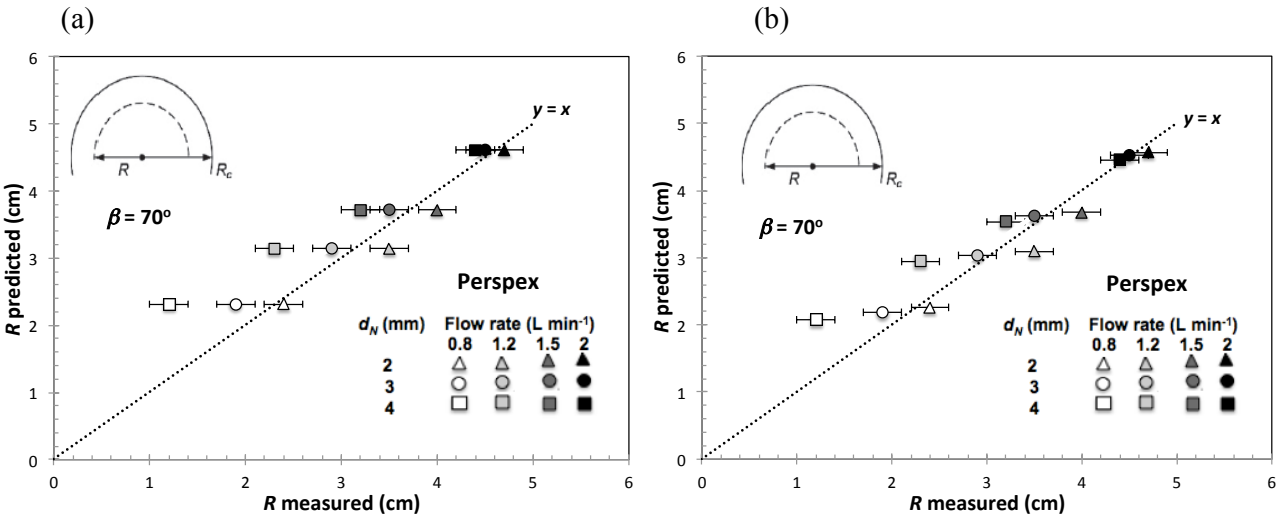

Figure 7. Comparison between theory and experiments for R on Perspex. (a) Equation (1). (b) Equation (2). Uncertainty in model parameters was small compared to the predicted values.

Figure 8 shows results using equation (2) for calculating R on glass and polypropylene. Relatively better agreement is depicted for glass when an effective contact angle of 90° is chosen in place of 36° (see Table 3). Wang *et al*. (2013a) explained that this effective contact angle could be justified by the presence of a transition from surface tension-dominated behaviour to an inertial regime where the influence of substrate decreases due to the use of relatively high flow rates. The flow rates employed in this project lie at the higher end of the range used by Wang *et al*. (2013a). Hence, at higher flow rates, the influence of contact angle weakens and a reasonable estimate for R can be obtained with an effective contact angle of 90°.

Another explanation could be related to the dynamic contact angle. The contact angles used in this project are static, although the dynamic ones should be used. As discussed in section 2, the dynamic advancing contact angle increases with liquid speed. Hence, the use of a 90° contact angle rather than 36° for water flowing on glass at high flow rates (i.e. high speeds) could be justified by this dynamic contact angle argument. For instance, Blake (2006) showed that the advancing contact angle of silicone oils on glass is 0° (complete wetting) in the static case and can reach 160° when the liquid speed is increased.

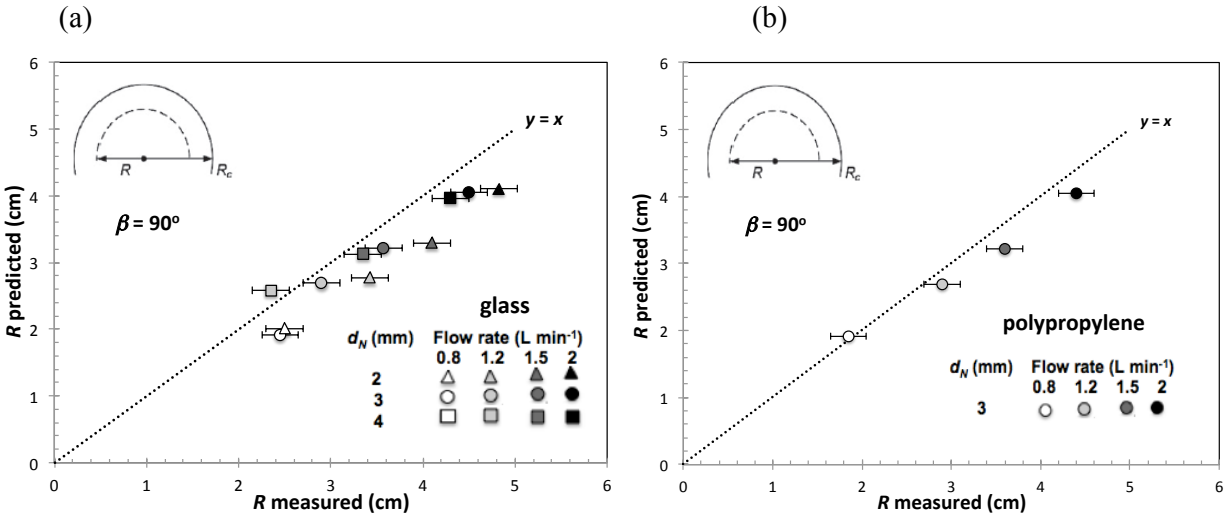

Figure 8. Comparison between theory (equation (2)) and experiments for *R* on (a) glass; (b) polypropylene. Uncertainty in model parameters was found small compared to the predicted values.

As for Z_r and Z_t, Figure 9 compares experimental results with the predictions of equations (3) to (7) on all substrates for a 3 mm nozzle. The model, which includes gravity, over-predicts the observed maximum height of the film jump Z_r. This can be explained by one feature that is not captured in the model: determining the location of Z_r experimentally is relatively hard since the flow at this level in the rope region is very unsteady and constantly fluctuates. This is most probably due to the fact that gravity opposes the radial momentum that is constantly supplied by the radial flow zone. Thus, there is a possibility of liquid falling back on top of the film flowing radially outwards. This will shift the observed location of Z_r towards the point of impingement (Wang *et al*. (2013b)). Another explanation for the fluctuation of the flow could be the presence of pulsations or instabilities coming from the pump or due to the presence of waves on the surface of the film. These waves can reach the interface between zones I and II and shift the position of the film jump since the wave speed is different from that of the bulk, based on the analysis of Bohr *et al*. (1996) for hydraulic jumps. Finally, splattering,

during which liquid splashes off the surface following impact, might occur due to the use of relatively high flow rates, which may cause changes in the local flow rate.

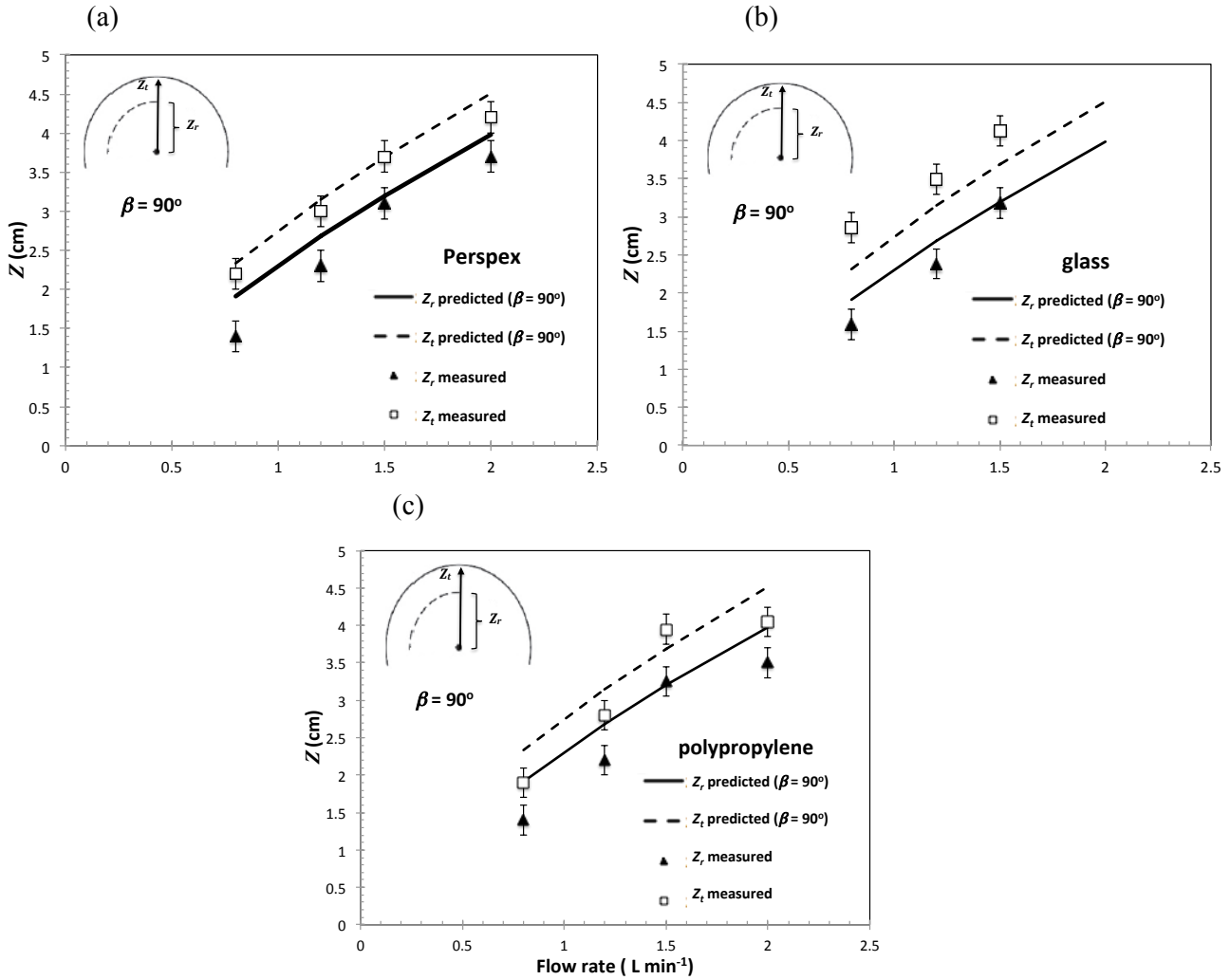

Figure 9. Comparison between theory and experiments for Z_r and Z_t using a 3 mm nozzle on (a) Perspex; (b) glass; (c) polypropylene.

Regarding Z_t, it is seen that there is a poor agreement between theory and experiments. Assuming that the rope has a semi-circular cross-section for equation (6) is likely to be invalid since gravity effects opposing the spreading are higher at the maximum height level than that at the mid-plane. As mentioned in section 5.2 for the Z_r, the flow in the rope is also quite chaotic and very unsteady.

An effective contact angle of 90° is found to give satisfactory fit between theory and experiments for all substrates, suggesting that the model becomes insensitive to the substrate nature at these higher flow rates.

PIV analysis

PIV experiments were conducted to determine the velocity distribution within the radial flow zone in order to evaluate the accuracy of the assumptions used to develop the models for R and Z_r. PIV provides information about the surface velocity and the trajectory taken by the particles.

A principal assumption used in the model is radial flow (i.e. the liquid streamlines are straight). Figure 10 shows the trajectory taken by the particles in the radial flow zone. The streamlines are approximately straight, which confirms the radial flow assumption in zone I. A few millimetres before reaching the interface between zones I and II, the particles start to slow down and the trajectory becomes slightly curved.

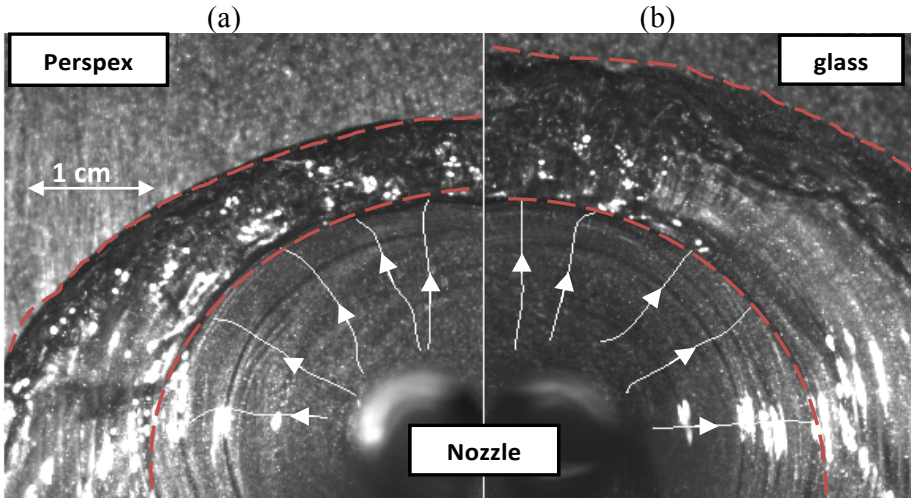

Figure 10. Trajectory of the particles in the radial flow zone. (a) q = 0.73 L min^{-1} on Perspex. (b) q = 0.71 L min^{-1} on glass. The arrows indicate the streamlines and the dashed lines show the boundary of zone II. d_N= 2 mm.

The models for R and Z_r also assume that the liquid flow follows a parabolic velocity profile, i.e. Nusselt thin film. Following the analysis of Nusselt (1916) for falling films, the local velocity u at depth z is:

$$u = U_s \left[2\left(\frac{z}{\delta}\right) - \left(\frac{z}{\delta}\right)^2 \right], \tag{26}$$

where δ is its thickness and U_s is the surface velocity.

The surface velocity U_s can be linked with the mean velocity of the film U using the following expression:

$$U_s = \frac{3}{2} U\,. \tag{27}$$

Figure 11 compares the radial velocity profiles predicted by the R and Z_r models with the surface velocities measured using PIV on Perspex. Results for glass showed similar trends. The average velocities from the models were converted to surface velocities using equation (27). The surface velocities derived from the R model (equation (3) by setting $\theta = 90^o$) and the Z_r model (equation (3) by setting $\theta = 0^o$) are symbolized by $U_{s,\theta}$. The models under-estimate the measured surface velocity of the film in the radial flow zone. However, waves are present in the flow as shown in Figure 10.

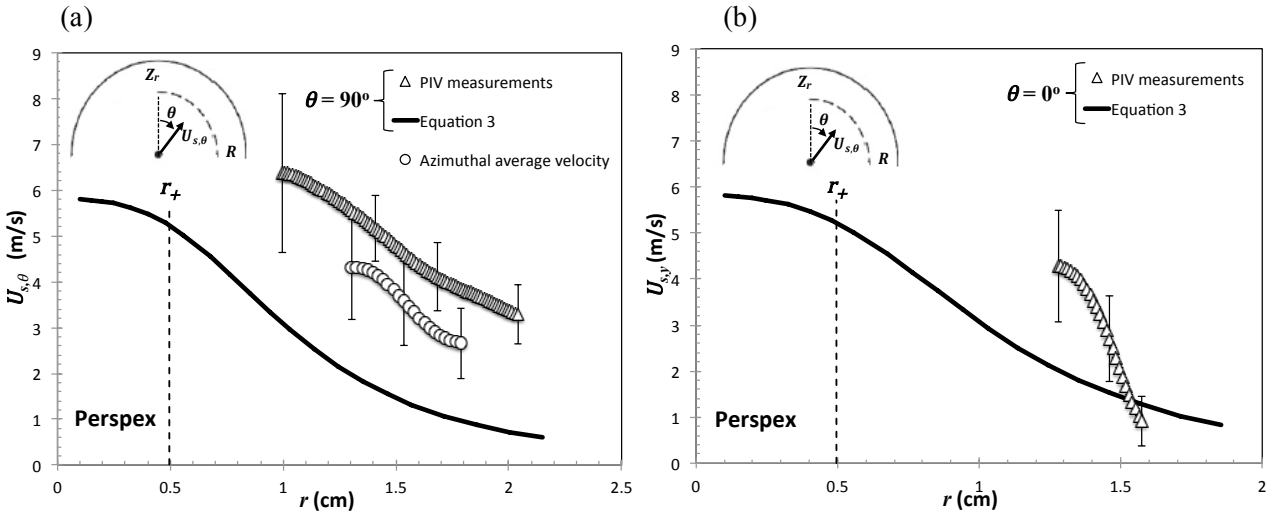

Figure 11. Comparison between the surface velocity profiles given by the R and Z_r models and the PIV measurements for q = 0.73 L min^{-1} on Perspex. (a) R model. (b) Z_r model. d_N= 2 mm. Dashed, vertical line shows the value of r_+ given by equation (28).

The steady parabolic flow condition requires the flow to be laminar, smooth and uniform. The film is relatively wavy and unsteady, as shown in Figure 10, whereas the Nusselt theory does not take into account the effects of even small waves on the liquid film.

Regarding the accuracy of the experimental results, some over-illumination at the mid-plane can be seen in Figure 10, which leads to an over-estimation of the velocity field. In order to supress any local constraint affecting the measurements, such as over-illumination, the measured surface velocities were averaged over the entire radial flow zone (called azimuthal average velocity), as shown in Figure 11 (a) (circles). The difference between the predicted and measured velocities is still present, although it becomes smaller.

It was hard to detect the particles in the region close to the impingement point, so no data were obtained for this region, shown by their absence in Figure 11 (below a distance of approximately 1

cm with respect to the radial distance r). This could be due to the presence of a high velocity field near the point of impingement, causing the particles to flicker and become hard to detect.

Critique of the derivation of equation (3) for the velocity profile in the radial flow zone

The region near the impingement point is relatively complex a discussed above. Yeckel and Middleman (2007) analysed the removal of a viscous film from a rigid plane surface by an impinging liquid jet. They found that outside of the impingement area, but within the film jump, two regions can be distinguished: the inner region, where the surface velocity is constant and the flow is governed by boundary layer growth, and the outer region, where the boundary layer has fully developed to include the whole flow. The velocity distribution in the inner region is constant (plug flow velocity profile rather than parabolic) and the boundary layer is still forming. The position of the transition between these two regions, r_+, is given by:

$$r_+ = 1.84\, r_0\, Re_{jet}^{1/9}\,. \tag{28}$$

Above this distance r_+, the velocity profile becomes parabolic, as assumed by Wilson *et al*. (2012) and Wang *et al*. (2013b). The value of r_+ is of the order of 0.5 cm and is shown in Figure 11 (dashed line), which corresponds to approximately 25-30% of the values of R and Z_r for the flow rate used in Figure 11. Hence, the assumption of a Nusselt film (parabolic velocity profile) used over the entire radial flow zone is not very accurate.

5.3 Zone II: predictions and measurements of R_c and Z_t for water

Critique of equations (5) and (6) for the calculation of Z_t

The analysis for Z_t was presented in section 5.2 above. As mentioned in section 2.2, the width of the rope (equation (5)) is obtained by setting θ in equations (5) and (6) to 1° (since 0° is mathematically impossible due to the presence of θ in the denominator). However, a Taylor expansion can be used to evaluate equation (6) for θ = 0°:

$$f(\theta) \approx -\frac{5\theta^4}{72} + \frac{\theta^2}{4} + 1\,. \tag{29}$$

If $\theta \rightarrow 0^o$, $f(\theta)$ has a value of 1. Hence, $D(\theta = 0^o)$ given by equation (5) becomes equal to 0 m.

This suggests that the rope at the maximum height of the film jump does not exist ($Z_t = Z_r$). This is not observed in practice as shown in Figure 10: Z_t and Z_r are distinct.

Regarding R_c, relatively good agreement is found between empirical relationships and experiments, as shown in Figure 12. Perspex and polypropylene (Figures 12 (a) and (c), respectively) gave good agreement between R_c and the empirical relationship $R_c \approx 4R/3$ for all flow rates. Wilson *et al*. (2012)

found similarly good agreement on Perspex for high flow rates but they did not study polypropylene. The flow rates in this study are similar to those used by Morison and Thorpe (2002). However, glass contradicts this observation since Figure 12 (b) shows that $R_c \approx 2R$ for water on glass. This is attributed to the high wetting behaviour of glass compared to the other substrates used.

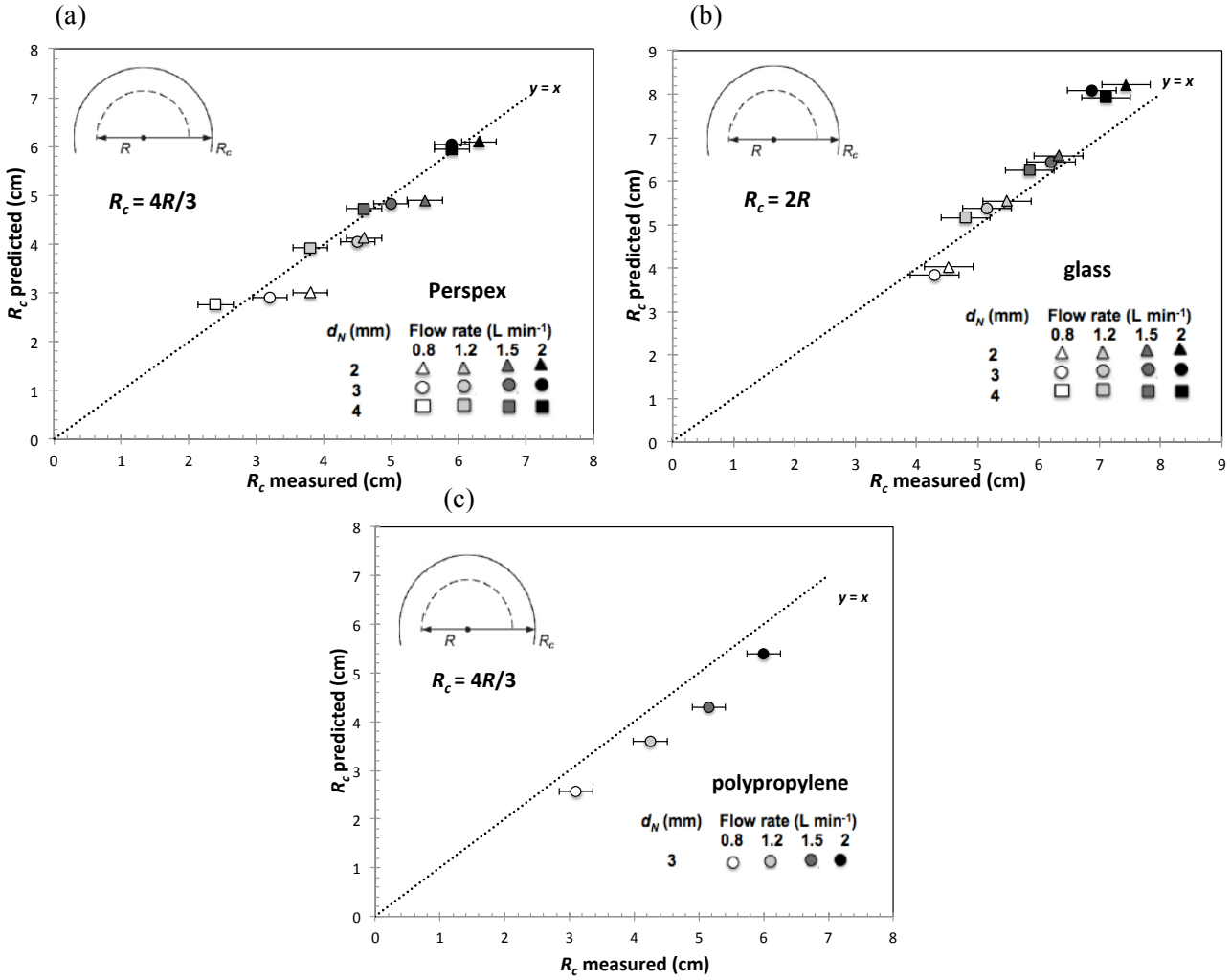

Figure 12. Comparison between empirical relationships and experiments for R_c on (a) Perspex: $R_c \sim 4R/3$; (b) glass: $R_c \sim 2R$; (c) polypropylene: $R_c \sim 4R/3$. Uncertainty in model parameters was found small compared to the predicted values.

5.4 Zone III: experimental result

The initial half width of the falling film, given by R_c, can be estimated reasonably well using the theoretical and empirical models presented in the sections above. The shape of the draining film in zone III is considered in Figure 13, which presents data illustrating the half width w at a downward

distance x below the impingement plane when gravity flow is observed. The half width is plotted as w/R_c, showing the width relative to that at the impingement level, whereas the downward distance x is illustrated as x/R for comparison with the distance relative to the radius of zone I.

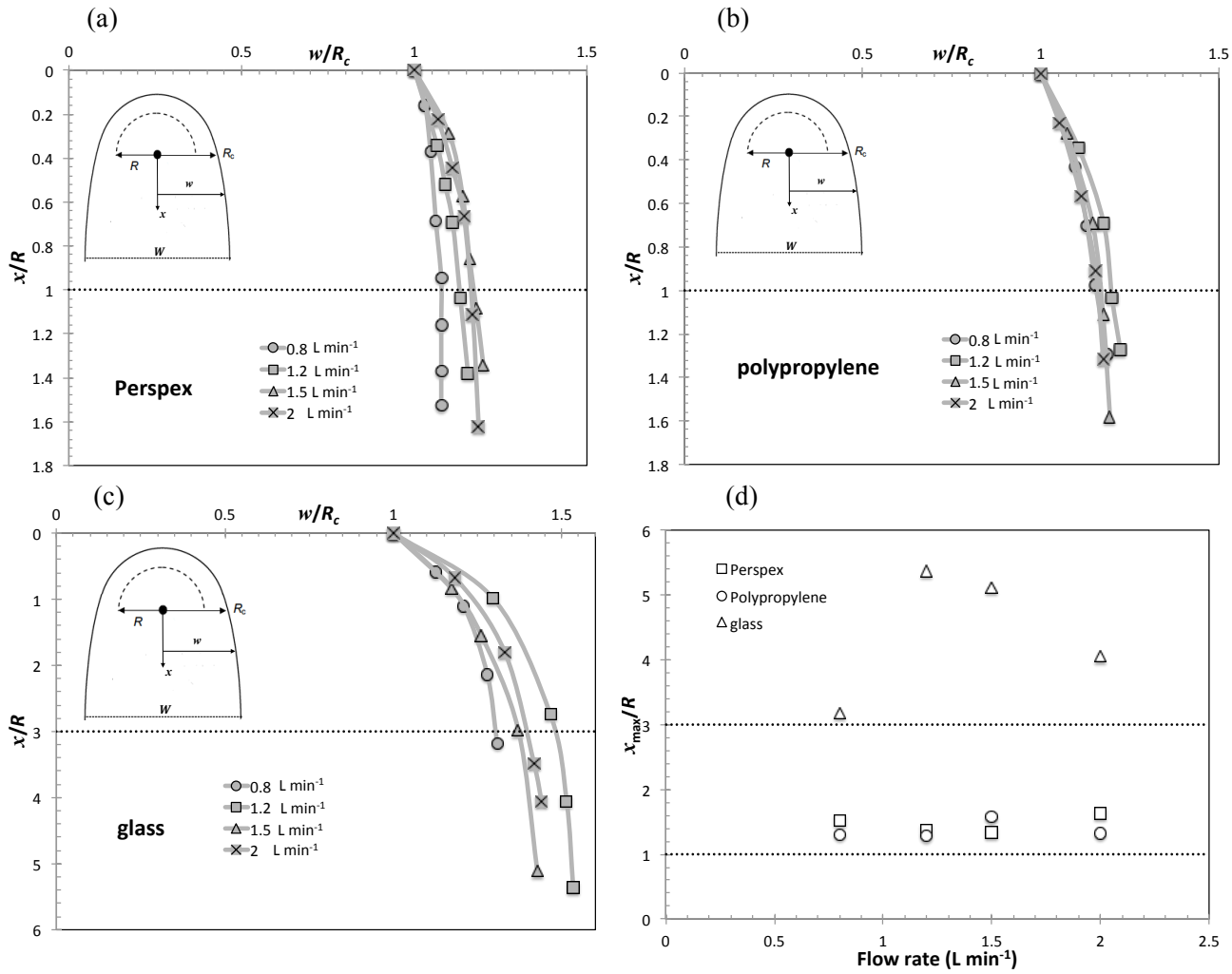

Figure 13. Draining film shapes in zone III for gravity flow of water on (a) Perspex; (b) polypropylene; (c) glass. (d) shows the maximum vertical extent of zone III, x_{max}, as a function of the flow rate on all substrates. The horizontal dashed line indicates the location where $x = R$ on Perspex and polypropylene, and $x = 3R$ on glass. d_N= 3 mm.

Results are shown for a nozzle diameter of 3 mm. The other diameters showed similar trends. A horizontal dashed line is marked on each plot at $x = R$ (Figures (a) and (b)) and $x = 3R$ (Figure (c)). Wang *et al*. (2013a) argued that the distance $x = R$ is approximately the maximum extent at which liquid is assumed to be added to the film, since the radial flow zone (zone I) is nearly symmetric (with respect to the mid-plane) within zone III. Thus, no horizontal momentum from the

impingement point is added to the liquid beyond a distance downward R, marking the start of zone IV.

Figures 13 (a) and (b) show that zone III extends downwards over a distance roughly equal to R to $2R$ for Perspex and polypropylene. However, water on glass exhibits a different behaviour: the width continues to increase over a distance x roughly equal to $3R$ to $5R$ as shown in Figure 13 (c). This means that horizontal momentum remains to be added to the liquid from the impingement point, or the flow takes time to adjust to the narrowing regime over this distance. The difference between the behaviour of zone III on glass and the other substrates is consistent with the results reported by Wang *et al*. (2013a) regarding the effect of surfactant on flow patterns and draining films created by a static horizontal liquid jet impinging on a vertical surface. They argued that the dynamic surface tension effects were not important in modelling the behaviour of zone I but were significant for the draining film zone. Hence, the wetting characteristics of the substrate, which are directly related to the contact angle and surface tension, play an important role in determining the behaviour of zone III. This analysis can clearly explain the results obtained in this zone: glass is substantially more wetting than the other substrates. Figure 13 (d) shows the maximum vertical extent of zone III, indicated by x_{max}, as a function of the flow rate and surface. It is seen that the behaviour of water on Perspex and polypropylene is similar, whereas water on glass exhibits a random behaviour. No clear effect of the flow rate is also depicted.

Moreover, the radial flow region in zone III is hard to observe in practice and a sharp film jump is not defined, unlike the radial flow zone (zone I) where the interface between this zone and the corona (zone II) can be better seen. This means that the radial flow within zone III is dependent on the wetting properties of the impact surface.

PIV analysis

PIV experiments were conducted to determine the surface velocity distribution in zone III. The velocity measurements were compared with the velocity profile that can be derived from the gravity model (equation (3)) by setting θ equal to 180^{o} ($\cos(\theta) = -1$), and equation (27) to convert to surface velocity. The downward surface velocity distribution is indicated by $U_{s,x}$. Figure 14 shows the results obtained for Perspex and glass.

It was hard to detect the particles in the region close to the impingement point for reasons similar to those reported above with zone I, so no data were obtained for this region as shown by their absence in Figure 14 for the first few centimetres.

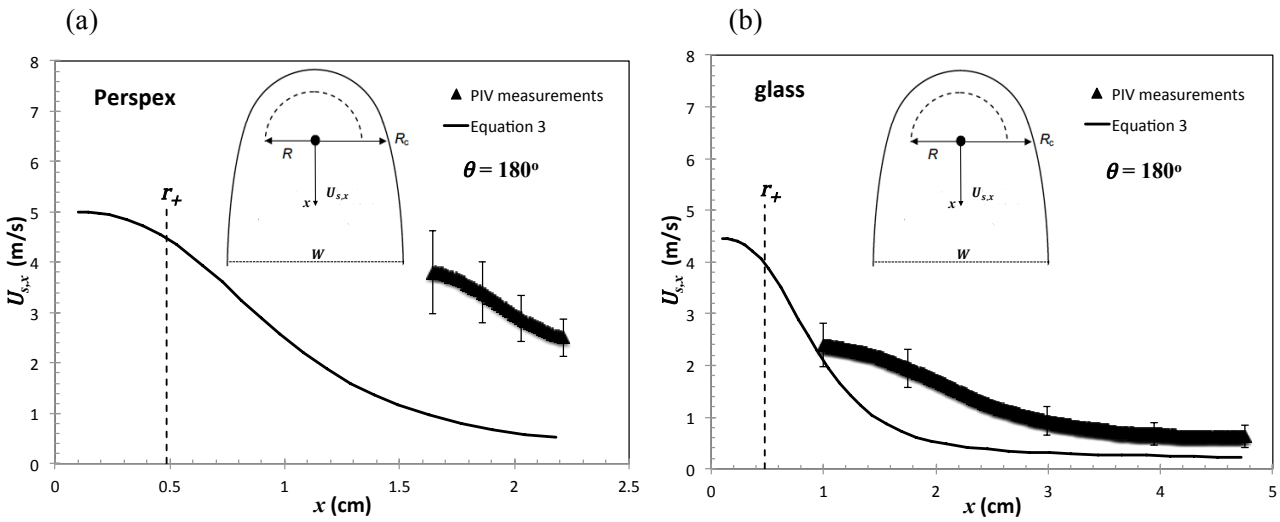

Figure 14. Comparison between the surface velocity profiles given by the gravity model (equation 3) and the PIV measurements in zone III for (a) q = 0.63 L min^{-1} on Perspex; (b) q = 0.56 L min^{-1} on glass. d_N= 2 mm. Dashed, vertical line shows the value of r_+ given by equation (28).

As with zone I, equation (3) under-estimates the velocity of the film in zone III. The explanation of this difference is similar to the one presented in section 5.2 regarding the velocity profiles in the radial flow zone (zone I).

5.5 Zone IV: comparison between the model and experiments for the narrowing width

The data in this region were compared with Mertens *et al.*'s model using the alternative capillary force (equation (25)) and Mertens *et al.*'s capillary force (equation (24)). These boundary conditions were used with equations (20) and (21) to give the half-width w as a function of x for modelling the narrowing width in zone IV. As mentioned in section 4, Matlab™ was used for modelling. The maximum width, which is one of the boundary conditions needed to solve equations (20) and (21), was measured experimentally for each combination of flow rate and surface by taking photographs of the flow (refer to section 4.1.3 for more details about the boundary conditions used). Figure 15 compares the predictions of the model for the 3 mm nozzle with the experimental observations of the narrowing shape on Perspex at different flow rates. It also shows the observed inner boundary of the rope region mentioned in section 4.1.3.

The narrowing pattern seems to be predicted well by the model using the alternative boundary condition (revised model). Good agreement is also found for water draining on glass and polypropylene (Figure 16). The contact angles used to obtain the best prediction in the modelling are 35°, 18° and 45° for Perspex, glass and polypropylene, respectively. As discussed above, the receding

contact angles should indeed be used in this zone of the flow. The values that gave the best fit are close to the measured receding contact angles in Table 3 (slightly higher) and are roughly half the average advancing contact angles. Hence, the guideline of using half of the advancing contact angle value seems to be a good starting point in the modelling process.

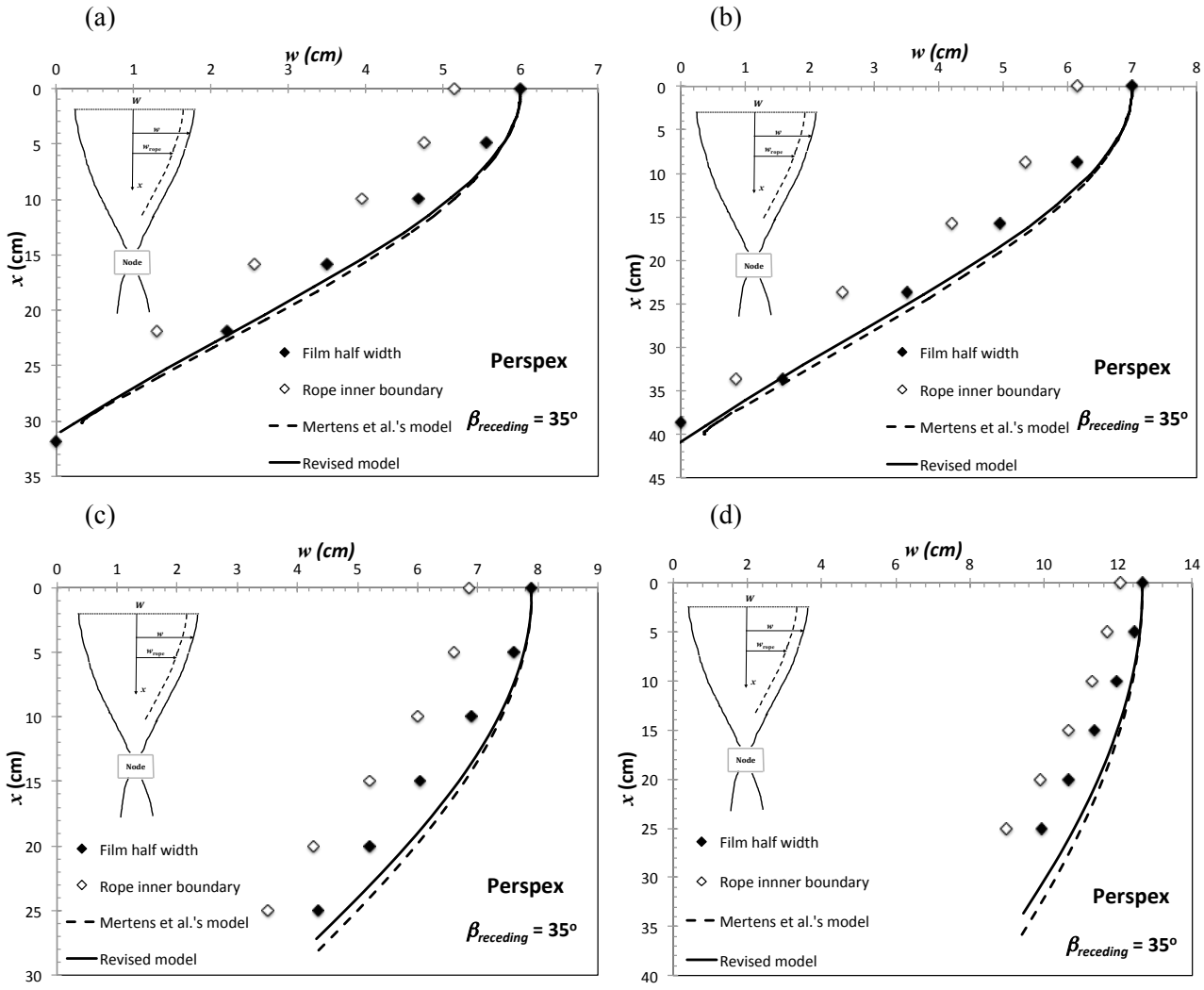

Figure 15. Comparison between theoretical predictions and experimental observations for zone IV for water on Perspex at (a) q = 1.5 L min^{-1}. (b) q = 2 L min^{-1}. (c) q = 2.3 L min^{-1}. (d) q = 4 L min^{-1}. d_N = 3 mm.

The rope region possesses a relatively constant width throughout zone IV as seen by the constant distance between the open and solid symbols. The results on polypropylene showed similar trends whereas the boundary of the rope was hard to identify on glass due to the shallow contact angle of water on this substrate.

The model is also able to predict the narrowing pattern at higher flow rates, (see Figures 15 (c) and (d)).

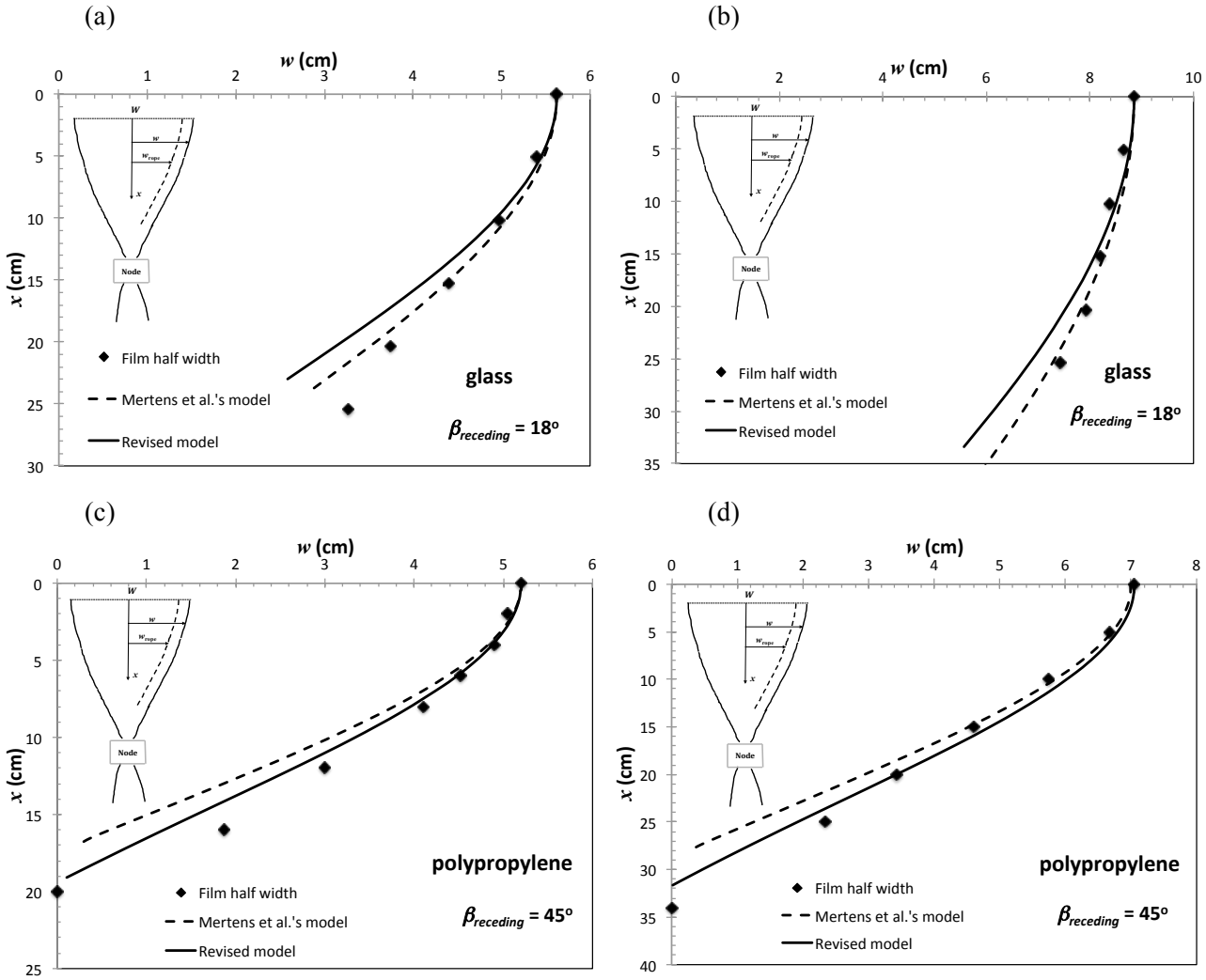

Figure 16. Comparison between theoretical predictions and experimental observations for zone IV for water on (a) glass at q = 0.8 L min^{-1}; (b) glass at q = 1.5 L min^{-1}; (c) polypropylene at q = 1.2 L min^{-1}; (d) polypropylene at q = 2 L min^{-1}. d_N = 3 mm.

Figures 15 and 16 also show the predictions of the model using Mertens *et al.*'s boundary condition (equation (24) for the capillary force). Equation (24) is able to predict the narrowing width as accurately as the alternative capillary force proposed in this project when the receding contact angle is used.

The bifurcation diagram, which characterizes the transition from rivulet to braiding (gravity) flow in terms of the dimensionless parameters Π_I and Π_{II} given by equations (22) and (23), is shown in

Figure 17 (see Mertens *et al.* (2005) for more details about this diagram). The transition line was taken as a power-law fit reported by Mertens *et al.*: $\Pi_{II} = 4.07\Pi_I^{1.89}$. The experimental data represent the values of Π_I and Π_{II} for the flow rates used in this study (0.48 to 4 L min^{-1}), which are similar to those employed by Mertens *et al* to observe the braiding pattern.

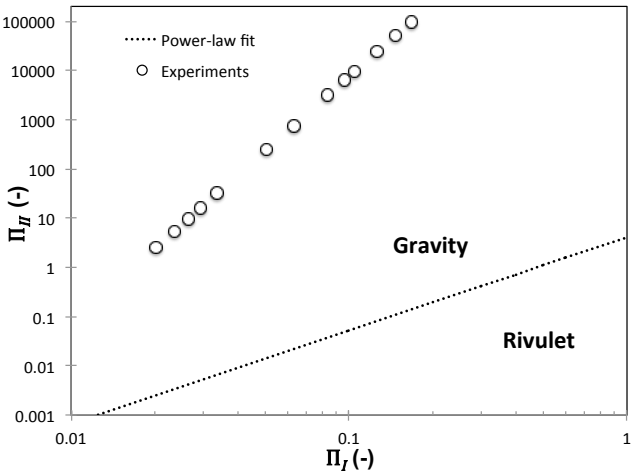

Figure 17. Experimental observations of braiding in terms of parameters Π_I and Π_{II}. Dotted line represents the power law fit indicating the transition from rivulet to braiding (gravity) flow.

The results show that all the experimental braiding observations lie within the zone predicted by Mertens *et al*. for the braiding pattern (the circles are located above the dotted transition line). Hence, the transition between rivulet and gravity flows based on the dimensionless parameters Π_I and Π_{II} was well predicted by Mertens *et al.* in their work.

PIV analysis

PIV measurements were made to evaluate the validity of the main assumptions used in Mertens *et al.*'s model, mentioned in section 4. One assumption is that the downward velocity, U_x, is uniform and independent of the horizontal position y. Figure 18 illustrates the downward surface velocity distribution, $U_{s,x}$, as a function of y at x = 3.23 cm on Perspex and x = 5.93 cm on glass in zone IV. The velocity profile as well as the half width predicted by the revised model at the same distances are also included. Good agreement is found between the velocity calculated by the model and the measured velocities in the central region. Moreover, the half width is predicted reasonably well.

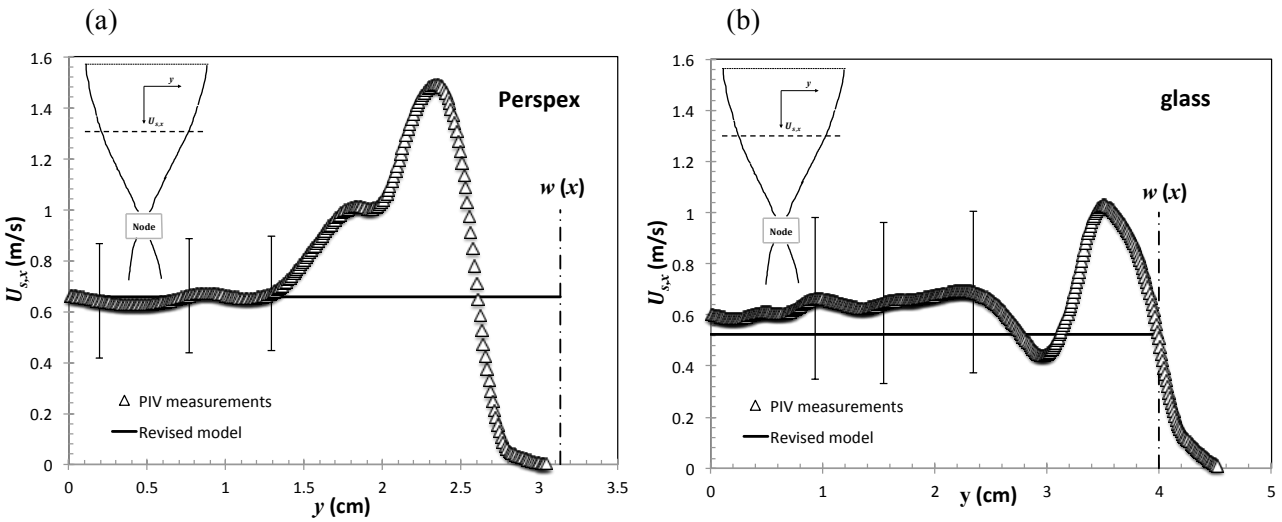

Figure 18. Downward surface velocity profile as a function of y for (a) q= 0.63 L min^{-1} on Perspex; (b) q = 0.56 L min^{-1} on glass. Dashed, vertical line shows predicted half width at this x value, and solid horizontal line shows predicted $U_{s,x}$ value.

Two regions can be distinguished. There is a relatively uniform velocity profile in the central region corresponding to the flat-shaped region mentioned in section 4.1.3. The second region near the edge has a non-uniform profile, corresponding to the ropes. This shows that the assumption of a uniform velocity in the y direction is not accurate. It is therefore important to know what fraction of the total flow is present in the central region.

Based on a simple geometric argument, the radial flow zone (zone I) should carry half of the flow into the corona (zone II) and then drain via the ropes, whereas the symmetric radial flow region in zone III, mentioned in section 5.4, should transport the other half of the flow. This argument assumes no exchange between the two regions. Wang *et al*. (2013b) used this construction to estimate the likelihood of dry patch formation. Hence, the ratio of the flow in the central region (q_F) to the total flow (q) as well as the ratio of the flow in the ropes (q_R) to the total flow (q) were calculated at random positions x in the draining film zone. This has been done assuming a Nusselt falling film: the surface velocity was measured using PIV and the average velocity was calculated using equation (27). Then, the thickness of the film was obtained from the surface velocity by isolating δ using the following equation based on the analysis done by Nusselt (1916) for falling films:

$$U_s = \frac{\rho g \delta^2}{2\mu}. \tag{30}$$

Similarly, the ratio of the flow in the ropes to the total flow was calculated by dividing the rope region into several vertical slices and by assuming Nusselt film behaviour in each interval since the

velocity profile is not uniform. Table 4 shows the results obtained for Perspex and glass at different flow rates.

Table 4. Analysis of the flow partitioning in falling film.

Substrate (-)	q (L min^{-1})	x (cm)	$2\times w$ (cm)	Width between ropes (cm)	q_F/q (%)	q_R/q (%)	Total (%)
Perspex	0.48	2.29	4.44	2.1	42 - 47	69	111 - 116
Perspex	0.63	3.23	5.87	3.40	52 - 58	78	130-136
Perspex	0.72	4.10	5.69	3.40	45 - 51	35	80 - 86
glass	0.56	5.94	7.6	4.6	70	53	123
glass	0.72	3.40	9.76	6.0	71	56	127

Table 4 indicates that the ratio between the flow in the central region and the total flow is close to 50% when the substrate is Perspex. With glass, q_F/q is consistently close to 70% but $q_R/q \approx 50\%$. Assuming a Nusselt film in the rope region is likely to be incorrect since the velocities are relatively high in this region (the simple gravity driven flow assumption may not apply). The flow in the ropes is unsteady and there is a possibility of recirculation within the ropes. Furthermore, judging the value of the velocities measured by PIV in the ropes is hard since this region is relatively thick and moves fast, which makes it difficult to detect the particles at the surface. Moreover, the central region is also unsteady and many waves are observed, which invalidates the Nusselt falling film analysis where the flow is considered to be laminar, smooth and uniform. Figure 19 shows the waves formed on the surface of the film, at low flow rates. The falling film is observed to be wavy and unstable.

Based on the experimental work of Chang (1994) on wave evolution in falling films, the film Reynolds number was calculated using the following expression:

$$Re = \frac{U\delta}{\nu}\ , \tag{31}$$

where δ is the Nusselt thickness of the film calculated using the Nusselt film analysis (equation 30). The mean film velocity U was calculated by converting the surface velocity in the central region of the film, given by the PIV measurements, using equation (27). Table 5 summarizes the results for the Reynolds numbers at random positions x (see Table 4 for these positions) in the falling film.

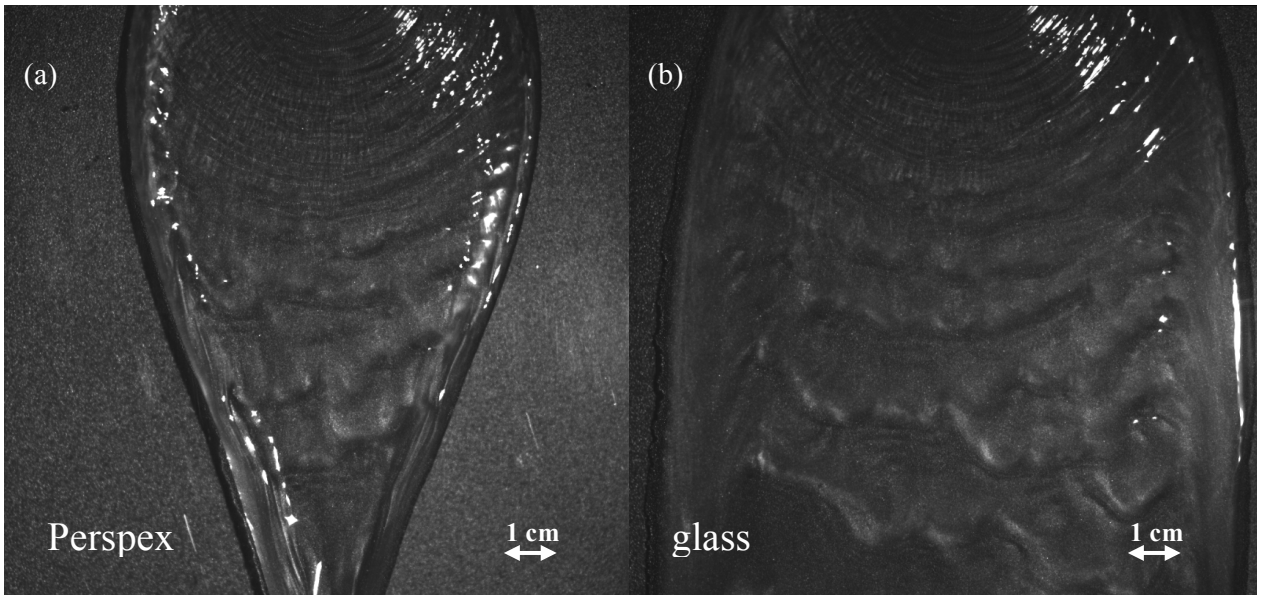

Figure 19. Surface wave formation in the falling film zone for q = 0.72 L min^{-1} on (a) Perspex; (b) glass.

Table 5 shows that the estimated Reynolds number is of the order of a hundred. According to Chang (1994), these correspond to the case where there is an instability in the film and consists of long interfacial waves dominated by gravity-capillary effects ($1 < Re < 300$). Based on the analysis of Dietze *et al*. (2008) for falling liquid films, backflow occurs in the capillary wave region because the wave velocity is considerably larger than the mean flow velocity in the bulk. Hence, the phenomena manifested in zone IV are more complex that the Nusselt analysis for a uniform and smooth film, as assumed by Mertens *et al*.

Table 5. Summary of the film Reynolds number in the falling film zone.

Substrate (-)	q (L min^{-1})	U_S, measured (m s^{-1})	δ, equation (30) (mm)	U, calculated (m s^{-1})	Re (-)
Perspex	0.48	0.65 – 0.70	0.37 – 0.38	0.43 – 0.47	155 - 174
Perspex	0.63	0.65 – 0.70	0.37 – 0.38	0.43 – 0.47	155 - 174
Perspex	0.72	0.65 – 0.70	0.37 – 0.38	0.43 – 0.47	155 - 174
glass	0.56	0.60	0.36	0.4	138
glass	0.72	0.60	0.36	0.4	138

Finally, the velocity profiles (converted to surface velocities using equation (27)) in the model for zone IV are compared with the PIV measurements in Figure 20.

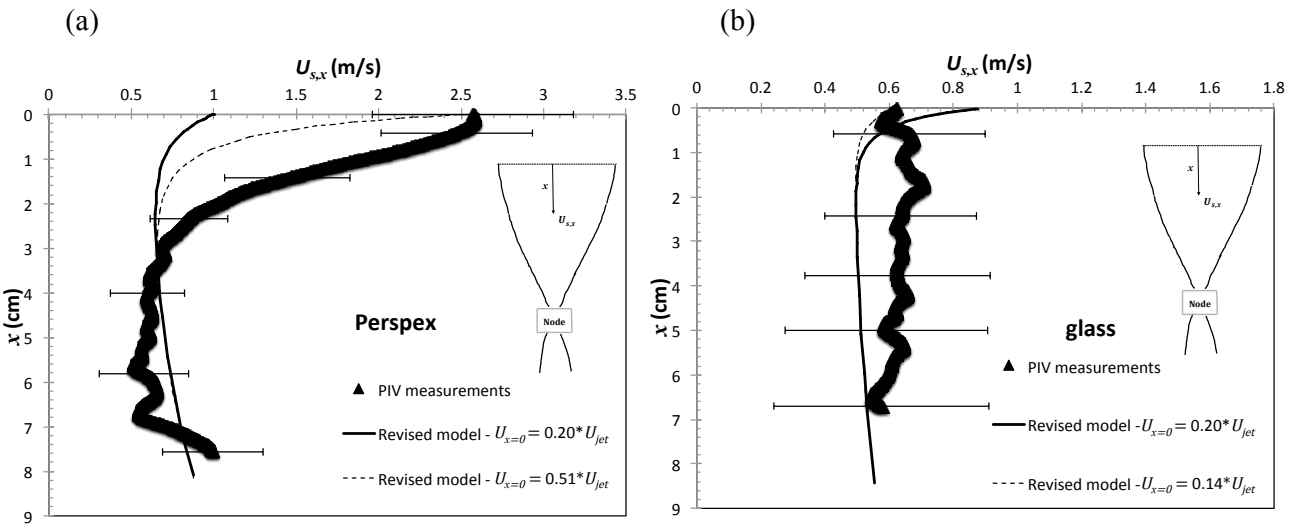

Figure 20. Comparison between surface velocity profiles predicted by the revised model and experiments at $y = 0$ for (a) $q = 0.63$ L min^{-1} on Perspex; (b) $q = 0.56$ L min^{-1} on glass.

The velocities derived from Mertens *et al.*'s model using the alternative capillary force (revised model) give a reasonable prediction of the experimental velocities. Nonetheless, the Nusselt film assumption may not be accurate due the formation of waves as discussed above. It is also clearly seen that close to the maximum width W ($x = 0$) for Perspex, the experimental measurements are higher than predicted. This can be explained by the fact that the maximum width position on Perspex is relatively close to the impingement zone due to the poor wetting behaviour of Perspex. Therefore, there might be some additional momentum from the radial flow zone. Hence, the gravity-driven flow (Nusselt falling film) assumption may not be accurate close to the maximum width level on Perspex.

Finally, Figure 20 shows that the assumption that the velocity at the maximum width position is equal to 20% of the jet velocity (see section 4.1.3 for boundary condition (*iii*)) is not very accurate. The PIV measurements indicate a value of 51% on Perspex (when $q = 0.63$ L min^{-1}) and a lower one on glass (14% when $q = 0.56$ L min^{-1}). The predictions of the revised model by changing boundary condition (*iii*) for each substrate are also given in Figure 20. In the absence of detailed knowledge, 20% seems to be a reasonable average percentage when modelling zone IV. The initial velocity value does not have a significant effect on the evolution of the film width in the draining film zone.

Regarding the accuracy of the PIV results, the speed of the waves can be detected in place of the speed of the particles in the film, which leads to an over-estimation of the experimental velocity profile since the waves travel faster than the bulk in falling films (Dietze *et al.* (2008)).

Qualitative analogy between the mechanism of braiding and the spring

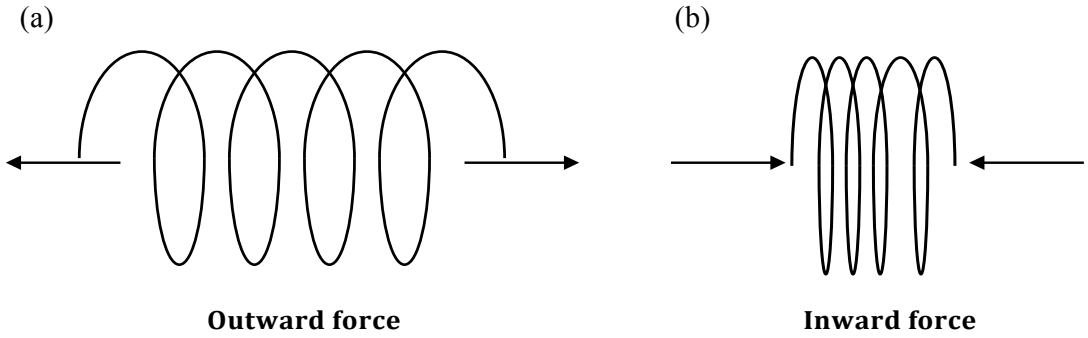

Figure 21. Schematic of outward and inwards forces acting on a typical spring.

An analogy is proposed in this study between the phenomenon of braiding and the reaction of a spring to an applied force. If the force is in the outward direction (Figure 21 (a)), the spring will store potential energy that will enable it to compress back once the applied force ends. In a similar fashion, it will stretch if the applied force is causing it to compress (Figure 21 (b)). Thus, the potential energy is converted into kinetic energy, enabling the spring to either stretch or compress until reaching its initial stable state. The more the spring is compressed (or stretched), the higher is the potential energy transformed into kinetic energy. This analogy can be used to explain the braiding pattern treated in this study. In zone III, radial momentum causes the flow to stretch, which is shown by an increase in width. Once the horizontal momentum dissipates (maximum width level), surface tension effects become dominant and the flow starts to narrow, similarly to a spring that is being compressed. As the width decreases, surface energy becomes smaller and the kinetic energy of the flow increases, due to the increase in the film thickness. The increase in thickness induces a flip in the flow surface, from a convex to a concave shape. This flip, in addition to the adverse pressure gradient, causes the ropes to bounce at the node level. After bouncing, kinetic energy becomes dominant and the film starts to widen until surface tension contributions become important again (maximum width level), similarly to a spring that is being stretched. The process is repeated and the braiding pattern is observed. Nonetheless, this pattern does not occur infinitely due to friction that dissipates the energy of the flow. This mechanism is similar to the observations of Bush and Hasha (2004) for the formation of fluid chains following the collision of laminar jets: fluid accumulates at the edges of the created film to form relatively thick rims at the boundaries. When these rims collide, they give rise to another thin film and the process is repeated. Therefore, the braiding mechanism could be described as a spring extending and compressing depending on the force applied, which is either dominated by surface (narrowing) or kinetic (widening) energy. A preliminary quantitative analysis, although not included in this report due to space constraints, also confirmed this analogy.

6.0 Conclusions and recommendations

Flow patterns created by a coherent horizontal liquid jet impinging on vertical Perspex, glass and polypropylene-covered surfaces were studied. Experiments and theoretical results were compared and discussed. The jets were generated by nozzles similar to those used in industrial cleaning, with diameters ranging from 2 to 4 mm. PIV experiments were conducted to depict the velocity field within the flow. Four zones were detected.

Zone I or radial flow zone: the radius R as well and maximum height, Z_r, of the film jump were predicted reasonably well by existing models. The results were found to be relatively insensitive to the effect of nozzle diameter. PIV measurements confirmed that the flow in this zone is radial as the streamlines taken by particles are relatively straight. The theoretical velocity fields from the models were found to give inaccurate prediction of the velocities. This could be due either to the assumptions in the models (Nusselt thin film etc.), or an artefact of the PIV experiments where over-illumination has been detected.

The rope or corona: empirical relationships between R and the outer radius of the corona at the impingement plane, R_c, were studied. The results for Perspex and polypropylene were found to be similar, whereas the ones on glass were different due to the strong wetting properties of water on glass. The maximum height of the corona, Z_t, was not predicted reasonably well by the model and the assumption of circular cross-section of the corona was questioned.

Zone III: this zone is characterized by a radial flow from the impingement point and by gravity effects becoming important. Zone III was studied experimentally in this project. Water on Perspex and polypropylene exhibited similar behaviour. PIV measurements were compared with predictions using equation (3). The results showed less agreement, indicating that equation (3) is unreliable when used for zone III.

Zone IV: this zone is also called the falling film zone where no further horizontal momentum is added from impingement point. The flow reaches a maximum width and starts to narrow for partially wetting surfaces. Mertens *et al.*'s model was found to give a negative film thickness due the quartic function assumed for the height distribution. This function only affects the capillary force causing the flow to narrow. Thus, an alternative capillary force was proposed, which gave a good prediction of the narrowing pattern and the velocity field. This boundary condition predicts the first braid only (until the first node is reached). Receding contact angles were used to predict the flow behaviour in this zone. The validity of the Nusselt falling film assumption was questionable due to the presence of waves on the falling film surface.

Future work should consider the numerical simulation of the flow in zone III: this is a complex flow and unlikely to be amenable to theoretical analysis. Further PIV or alternative visualisation techniques should also be considered, e.g. laser sheets that allow the film thickness to be studied. Finally, extension of these results to moving impinging jets (where the nozzle traverses the surface) should be investigated since most of the cleaning processes in industry use rotating systems.

7.0 Nomenclature

Roman

A	Half cross-sectional area of liquid film at a given x	m^2
a	Constant in the height function, $h(x, y)$	m^{-1}
b	Constant in the height function, $h(x, y)$	m^{-3}
D	Rope width	m
d_N	Nozzle diameter	mm
F	Capillary force acting on the half-braid	N m^{-1}
F_*	Dimensionless form of the capillary force	N m^{-1}
g	Gravitational acceleration	m s^{-2}
h	Thickness of the film in the draining zone	m
H	Contact angle hysteresis	^{o}
l	Distance between the nozzle and the impact surface	cm
L	Characteristic length	m
$\dot{m}$	Mass flow rate	kg s^{-1}
PIV	Particle image velocimetry	-
q	Total flow rate	m^3 s^{-1}
q_F	Flow rate in the central region of the falling film	m^3 s^{-1}
q_R	Flow rate in the rope region of the falling film	m^3 s^{-1}
Q	Half flow rate	m^3 s^{-1}
RFZ	Radial flow zone	-
R	Radius of film jump at mid plane	m
R_c	Outer radius of flow at mid plane	m
r_o	Jet radius	m
r	Radial co-ordinate	m
r_+	Transition radius between the inner and outer regions in RFZ	m
Re_{jet}	Jet Reynolds number	-
Re	Falling film Reynolds number	-
U_o	Initial film mean velocity	m s^{-1}
U_R	Film mean velocity at R	m s^{-1}
U	Mean velocity in film	m s^{-1}
$\boldsymbol{U}$	Three-dimensional velocity vector	m s^{-1}
U_x	Velocity of the draining film in the x direction	m s^{-1}
u_*	Dimensionless form of U_x	-
u	Local velocity at depth z given by Nusselt (1916)	m s^{-1}
U_y	Velocity of the draining film in the y direction	m s^{-1}
U_s	Surface velocity of the film	m s^{-1}
$U_{s,\theta}$	The radial surface velocity in RFZ	m s^{-1}

$U_{s,x}$	The downward surface velocity in the falling film	m s^{-1}
V	Characteristic velocity	m s^{-1}
W	Maximum width	m
w	Half width	m
w_*	Dimensionless half width	-
x_*	Dimensionless x	-
x_{max}	The maximum extent of zone III	m
Z_r	Maximum height of the film jump	m
Z_t	Maximum height of the film above the point of impingement	m
Greek		
β	Contact angle	o
α	Angle of inclination of the plane	o
θ	Angle of liquid streamline from vertical	o
γ	Surface tension	N m^{-1}
ρ	Liquid density	kg m^{-3}
v	Kinematic viscosity	m^2 s^{-1}
μ	Dynamic viscosity	Pa s
Π_I	Dimensionless group in Equation (20)	-
Π_{II}	Dimensionless group in Equation (21)	-
δ	Nusselt thickness of the falling film	m

8.0 References

Birch, W., Carré, A. and Mittal, K.L, (2008). Developments in Surface Contamination and Cleaning. William Andrew, Inc, pp. 693–723.

Blake, T.D., (2006). The physics of moving wetting lines. *Journal of Colloids and Interface Science*, vol.299, pp. 1–13.

Bohr, T., Ellegaard, C., Hansen, A.E., Haaning, A., (1996). Hydraulic jumps, flow separation and wave breaking: An experimental study. *Physica B*, vol. 228, pp. 1-10.

Bush, J.W.M, Hasha, A.E, (2004). On the collision of laminar jets: fluid chains and fishbones. *Journal of Fluid Mechanics*, vol. 511, pp. 285–310.

Chang, H-C., (1994). Wave evolution on a falling film. *Annual Review of Fluid Mechanics,* vol. 26, pp. 103–136.

Chibowski, E., (2007). On some relations between advancing, receding and Young's contact angles. *Advances in Colloid and Interface Science*, vol. 133, pp. 51–59.

Chibowski, E., (2003). Surface free energy of a solid from contact angle hysteresis. *Advances in Colloid and Interface Science*, vol. 103, pp. 149–172.

Dalziel, S.B., Carr, M., Sveen, J.K. and Davies, P.A., (2007). Simultaneous synthetic Schlieren and PIV measurements for internal solitary waves. *Measurement Science and Technology*, vol. 18, pp. 533–547.

Davis, M.L., (2010). *Water and wastewater engineering: Design principles and practice*. McGraw-Hill, Dubuque.

de Gennes, P.G., (1985). Wetting: statics and dynamics. *Review of Modern Physics*, vol. 57 (3), Part I, pp. 827–863.

Detry, J.G., Deroanne, C., Sindic, M. and Jensen, B.B.B., (2009). Laminar flow in radial flow cell with small aspect ratios: Numerical and experimental study. *Chemical Engineering Science*, vol. 64, pp. 31–42.

Dietze, G. F., Leefken, A. and Kneer, R., (2008). Investigation of the backflow phenomenon in falling liquid films. *Journal of Fluid Mechanics*, vol. 595, pp. 435–459.

Jensen, B.B.B., (2014). Industrial cleaning flows – Knowledge gap in tank cleaning. *Fouling & Cleaning in Food Processing 2014*, Cambridge, United Kingdom, p. 298.

Jensen, B.B.B., Nielsen, J.B., Falster-Hansen, H. and Lindholm, K-A.Tank cleaning technology: Innovative application to improve clean-in-place (CIP). Yearbook 2011-12, European Hygienic Engineering and Design Group (EHEDG), pp. 26–30, Frankfurt.

Landel, J.R. and Dalziel, S.B., (2014). Cleaning of viscous drops on a flat inclined surface using gravity-driven film flows. *Fouling & Cleaning in Food Processing 2014*, Cambridge, United Kingdom, pp. 324–331.

Landel, J.R. and Dalziel, S.B., (2013). The fluid mechanics of decontamination processes. DAMTP Technical Report.

Le Grand, N., Daerr, A. and Limat, L., (2005). Shape and motion of drops sliding down an inclined plane. *Journal of Fluid Mechanics*, vol. 541, pp. 293–315.

Mertens, K., Putkaradze, V. and Vorobieff, P., (2004). Braiding patterns on an inclined plane. *Nature*, vol. 430, p. 165.

Mertens, K., Putkaradze, V. and Vorobieff, P., (2005). Morphology of a stream flowing down an inclined plane. Part 1. Braiding. *Journal of Fluid Mechanics*, vol. 531 (1), pp. 49–58.

Morison, K.R. and Thorpe, R.J., (2002). Liquid distribution from cleaning-in-place sprayballs. *Food and Bioproducts Processing,* vol. 80, pp. 270–275.

Nusselt, W., (1916). Oberflachen kondensation des wasserdampfes. *Zeitschrift des Vereines Deutscher Ingenieure*, vol. 60, pp. 541–546 (and 569–575).

Paramalingam, S., Winchester, J., and Marsh, C., (2000). On the fouling of falling film evaporators due to film break-up. *Food and Bioproducts Processing*, vol. 78 (C), pp. 79–84.

Tan, J., (2012). Surface Flow Modelling. M.Phil. Research Project Report. *University of Cambridge*.

Vargaftik, N. B., Volkov, B. N., and Voljak, L. D., (1983). *International Tables of the Surface Tension of Water*. American Chemical Society and the American Institute of Physics for the National Bureau of Standards Washington, DC.

Wang, T., (2014). Flow and cleaning behaviour of stationary coherent liquid jets impinging on vertical walls. PhD dissertation. *University of Cambridge*.

Wang, T., Davidson, J.F. and Wilson, D.I., (2013a). Effect of surfactant on flow patterns and draining films created by a static horizontal liquid jet impinging on a vertical surface at low flow rates. *Chemical Engineering Science*, vol. 88, pp.79–94.

Wang, T., Faria, D., Stevens, L.J., Tan, J.S.C., Davidson, J.F. and Wilson, D.I., (2013b). Flow patterns and draining films created by horizontal and inclined coherent water jets impinging on vertical walls. *Chemical Engineering Science*, vol. 102, pp. 585–601.

Watson, E.J.,(1964).The radial spread of a liquid jet over a horizontal plane. *Journal of Fluid. Mechanics*, vol. 20 (3), pp. 481–499.

Wilson, D.I., (2005). Challenges in cleaning: recent developments and future prospects. *Heat Transfer Engineering*, vol. 26 (1), pp. 51–59.

Wilson, D.I., Le, B.L., Dao, H.D.A., Lai, K.Y., Morison, K.R. and Davidson, J.F., (2012). Surface flow and drainage films created by horizontal impinging liquid jets. *Chemical Engineering Science*, vol. 68, pp. 449–460.

Yeckel, A. and Middleman, S., (2007). Removal of a viscous film from a rigid plane surface by an impinging liquid jet. *Chemical Engineering Communications*, vol. 50, pp. 165-175.

Yu, H., (2013). Draining films generated by liquid jets impinging on vertical walls. M.Phil. Research Project Report. *University of Cambridge*.

Zografi, G. and Johnson, B. A., (1984). Effects of surface roughness on advancing and receding contact angles. *International Journal of Pharmaceutics*, vol. 22, pp.159–176.